INSTITUTO SUPERIOR DE ENGENHARIA DO PORTO
MESTRADO EM ENGENHARIA BIOMÉDICA



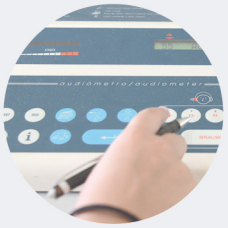


Transmissão de feixes laser de intensidade modulada em tecidos biológicos e a sua optimização

GONÇALO OLIVEIRA RODRIGUES
outubro de 2025

P.PORTO

ISEP INSTITUTO SUPERIOR DE ENGENHARIA DO PORTO

Transmission of intensity-modulated laser beams in biological tissues and their enhancement

Gonçalo Oliveira Rodrigues

Dissertation for obtaining a Master's Degree in Biomedical Engineering

Orientador: Luís Manuel Oliveira

Coorientador: Maria Inês Carvalho

Júri:

Presidente:

Joaquim Fernando Almeida Alves, Professor Adjunto, ISEP

Vogais:

Luís Manuel Couto de Oliveira, Professor Adjunto, ISEP

Luís Manuel de Sousa Pessoa, Professor Auxiliar, FEUP

Porto, September 2025

"Whatever makes you uncomfortable is your biggest opportunity for growth."

Bryant H. McGill

Resumo

Este trabalho foca-se no estudo da transmissão de feixes laser com intensidade modulada em tecidos biológicos, com ênfase no tecido muscular esquelético, e na forma como a aplicação de tratamentos de transparência pode melhorar essa transmissão. O trabalho surge no contexto do crescente interesse por técnicas óticas não invasivas na área da medicina, substituindo métodos baseados em radiação ionizante, como a tomografia computorizada, por alternativas mais seguras e eficazes. A Ótica Médica, disciplina que combina princípios de física, ótica e engenharia para aplicações médicas, tem permitido um avanço significativo em técnicas de diagnóstico e terapia baseadas na luz. No caso dos lasers, estes oferecem vantagens claras como emissão em comprimentos de onda específicos, feixes colimados, alta coerência e a possibilidade de modulação de intensidade ou emissão em modo pulsado. Estes atributos fazem com que os lasers sejam ferramentas poderosas tanto para procedimentos de diagnóstico como de tratamento, de que são exemplo a fotocoagulação e a ablação de tumores em tecidos. No entanto, devido às propriedades de absorção e de espalhamento que são características dos tecidos, a luz laser perde intensidade e colimação de feixe com o aumento da profundidade nos tecidos. Na grande maioria dos tecidos biológicos, o espalhamento é sempre superior à absorção, sendo esta diferença tanto maior quanto menor for o comprimento de onda. Tal forte espalhamento deve-se em grande parte à constituição heterogénea dos tecidos e ao desfasamento localizado de índices de refração. A técnica de transparência ótica surge como solução para minimizar o espalhamento da luz e aumentar a transparência dos tecidos, através da substituição parcial ou integral da água intersticial e celular por um ou mais agentes de transparência, o que promove uma adaptação de índices de refração, tornando o tecido mais homogéneo oticamente e, por conseguinte, mais transparente.

Neste estudo, foram utilizados quatro agentes de transparência ótica: a sacarose, a glicerina, o líquido de cigarros eletrónicos e a tartrazina. Cada um destes agentes foi testado quanto à sua capacidade de criar transparência temporária em amostras de músculo esquelético de coelho, com o objetivo de avaliar a melhoria da transmissão de feixes laser com intensidade modulada, com comprimentos de onda entre os 400 e os 900 nm. A metodologia experimental utilizada consistiu na utilização de duas montagens experimentais de medição da transmitância. A primeira dessas montagens foi usada para medir espectros entre 200 e 1000 nm, que permitiram calcular as principais propriedades óticas espectrais do tecido muscular, assim como das soluções dos agentes de transparência utilizados. As propriedades óticas

espectrais obtidas foram o coeficiente de absorção e a dispersão anómala do músculo e das soluções, tendo-se obtido adicionalmente e apenas para o músculo o coeficiente de espalhamento. A segunda montagem experimental foi usada para medir a transmitância de feixes laser com intensidade modulada em tecido muscular, antes e após a criação de transparência, para quantificar essa transparência a cada comprimento de onda dos lasers usados. Os lasers utilizados nesta montagem experimental apresentam comprimentos de onda entre os 400 e 900 nm, e a modulação de intensidade foi realizada com um chopper ótico, sendo a deteção do feixe transmitido feita com um osciloscópio. Com a medição dos espectros das soluções dos agentes de transparência usados e do tecido muscular, foi possível calcular as propriedades óticas espectrais correspondentes, dados que permitirão justificar as transparências criadas no músculo em cada tratamento.

Os resultados obtidos revelaram que todos os agentes de transparência usados produziram efeitos visíveis, mas com eficiências diferentes. O maior aumento de transparência no músculo foi criado pela tartrazina, tendo-se observado um aumento intermédio para os tratamentos com o líquido de cigarros eletrónicos e com a glicerina e um menor resultado para o tratamento com sacarose. No caso do tratamento com tartrazina, não foi observada a criação de transparência para os lasers com emissão a 405 e a 532 nm. Isto porque a esses comprimentos de onda, a tartrazina apresenta uma forte absorção. Do ponto de vista experimental, foi possível quantificar a eficiência de transparência criada por cada agente, permitindo realizar uma análise comparativa entre os diferentes agentes de transparência e identificar janelas de transparência espectral relevantes para aplicações clínicas.

Este estudo fornece informação importante para o desenvolvimento de novas metodologias clínicas menos invasivas, através da utilização de feixes laser com intensidade modulada combinados com a criação de transparência, que permitirão otimizar procedimentos de diagnóstico e tratamento. Em suma, este trabalho destaca o papel fundamental dos efeitos de transparência em tecidos biológicos para aumentar a transmissão de feixes laser com intensidade modulada a maiores profundidades dentro dos tecidos, abrindo caminho para aplicações mais seguras, rápidas e eficazes na prática clínica moderna.

Palavras-chave: Tecidos biológicos, Laser com intensidade modulada, Absorção, Espalhamento, Tratamentos de transparência, Controlo das propriedades óticas de tecidos

Abstract

This work focuses on the study of the transmission of intensity-modulated laser beams in biological tissues, with an emphasis on skeletal muscle tissue, and on how the application of optical clearing treatments can improve such transmission. This work arises in the context of the growing interest in non-invasive optical techniques in the medical field, with safer and more effective alternatives to methods that use ionizing radiation, such as computed tomography. Biophotonics, a research field that combines principles of physics, optics, and engineering to develop innovative medical applications, has enabled significant advances in diagnostic and therapeutic techniques based on light. In the case of lasers, they offer clear advantages such as emission at specific wavelengths, collimated beams, high coherence, and the possibility of intensity modulation or pulsed mode emission. These attributes make lasers powerful tools for both diagnostic and treatment procedures, such as photocoagulation and tumor ablation in tissues. However, due to the absorption and scattering properties that are characteristic of tissues, laser light loses intensity and beam collimation with increasing light-probing depth in the tissues. In the vast majority of biological tissues, scattering is always greater than absorption, and this difference is even greater at shorter wavelengths. Such strong scattering is largely due to the heterogeneous composition of tissues and the localized refractive index mismatch. The optical clearing technique emerges as a solution to minimize light scattering and increase tissue transparency, through the partial or total replacement of interstitial and cellular water with one or more clearing agents, which promotes refractive index matching, making the tissue optically more homogeneous and, consequently, more transparent.

In this study, four optical clearing agents were used: sucrose, glycerol, electronic cigarette fluid, and tartrazine. Each of these agents was tested for its ability to create temporary transparency in samples of rabbit skeletal muscle, with the aim of evaluating the improvement in the transmission of intensity-modulated laser beams, with wavelengths between 400 and 900 nm. The experimental methodology used in this study consisted of two experimental setups for measuring transmittance. The first of these setups was used to measure spectra between 200 and 1000 nm, which allowed the calculation of the main spectral optical properties of muscle tissue, as well as the absorption spectra of the solutions of optical clearing agents used. The spectral optical properties obtained were the absorption coefficient and the anomalous dispersion of the muscle and the solutions of optical clearing agents , as well as the scattering coefficient of the muscle. The second experimental setup was used to measure the

transmittance of intensity-modulated laser beams in muscle tissue, before and after clearing, in order to quantify that transparency at each laser wavelength used. The lasers used with this experimental setup had wavelengths between 400 and 900 nm, and the intensity modulation was performed with an optical chopper, being the transmitted beam detected using an oscilloscope. By measuring the spectra of the tissue and the optical clearing agents solutions, it was possible to calculate their spectral optical properties, which were then used to explain the transparencies observed in muscle after each treatment.

The results obtained revealed that all the clearing agents used produced visible transparency effects, but with different efficiencies. The maximum increase in muscle transparency was created by tartrazine, with an intermediate increase observed for treatments with the electronic cigarette fluid and glycerol, and a lower transparency increase obtained for the treatment with sucrose. In the treatment with tartrazine, no transparency was observed for lasers emitting at 405 and 532 nm. This observation is due to the strong absorption that tartrazine presents in this spectral range. From an experimental point of view, it was possible to quantify the optical clearing efficiency created by each agent, allowing a comparative analysis between the different transparency agents and the identification of relevant spectral transparency windows for clinical applications. Changes in anomalous dispersion profiles were also observed, as a result of the structural reorganization of the tissues and interactions with the clearing agents.

This study provides important information for the development of innovative and less invasive clinical methodologies, through the use of intensity-modulated laser beams when combined with optical clearing treatments, which will allow the optimization of diagnostic and treatment procedures. In short, this work highlights the fundamental role of the transparency effects in biological tissues to allow higher transmission of intensity-modulated laser beams to bigger tissue depths, paving the way for safer, faster, and more effective applications in modern clinical practice.

Keywords: Biological tissues, Modulated intensity of laser, Absorption, Scattering, Optical clearing treatments, Control of tissue optical properties

Acknowledgements

First of all, I would like to express my genuine thanks to all those who supported and guided me throughout this project. This achievement would not have been possible without the invaluable contributions of many individuals.

To my supervisors, Professor Luís Oliveira and Professor Inês Carvalho, I would like to express my deepest thanks for placing their trust in me and my work. I am extremely grateful for their unconditional support, valuable guidance, and all the knowledge shared with me. Their exemplary mentorship has been truly inspiring and instrumental throughout this journey.

To my lab colleague, Rosário Pinheiro, I would like to express my gratitude for her constant willingness to assist me during the measurements, for her support in addressing all the questions that arose, and for the many moments we shared throughout this journey.

To my friends, I express my profound thanks for their companionship and support during this journey. The moments we shared have definitely helped make this process more manageable and pleasant.

To my parents and brothers, I extend my heartfelt thanks for their unwavering support and constant encouragement to be the best version of myself. This achievement is, in many ways, also theirs because they instilled in me the right values and determination that have guided me throughout this journey. I am also thankful to the rest of my family for their belief in my abilities and for always standing by me.

Finally, I am grateful to the Institute for Systems and Computer Engineering, Technology and Science (INESC TEC) for their warm reception and for providing the essential resources and facilities that supported the successful execution of my research.

Index

List of Figures

List of Tables

Acronyms and Symbols

List of Acronyms

Ab	Absorbance
CT	Computed Tomography
E-cig	Electronic Cigarette
ISF	Interstitial Fluid
K-K	Kramers-Kronig
LED	Light-emitting Diode
LLLT	Low-level Laser Therapy
MRI	Magnetic Resonance Imaging
NIR	Near-infrared
OCA	Optical Clearing Agent
OC	Optical Clearing
OC_{eff}	Optical Clearing Efficiency
OCT	Optical Coherence Tomography
RBCs	Red Blood Cells
RI	Refractive Index
R_t	Total reflectance
SHG	Second Harmonic Generation
T_c	Collimated Transmittance
T_t	Total transmittance
THz	Terahertz
TZ	Tartrazine
UV	Ultraviolet

List of Symbols

μ_a	Absorption coefficient
μ_s	Scattering coefficient
μ_t	Attenuation coefficient
$\boldsymbol{\rho}$	Density
$\boldsymbol{Vpp}$	Peak-to-Peak Voltage
$\boldsymbol{Vpp_{noise}}$	Peak-to-Peak noise Voltage
$\boldsymbol{Vpp_{laser}}$	Peak-to-Peak reference Voltage of laser

Chapter 1 – Introduction

1 Introduction

The present document includes the current state-of-the-art related to the applications of intensity-modulated laser beams, a detailed description of the methodology used in this work, the obtained results and their discussion, as well as the possible outcomes of the research that was conducted in the context of the Thesis/Dissertation curricular unit, part of the Master's Degree in Biomedical Engineering at the Polytechnic Institute of Porto - School of Engineering. All the necessary experimental studies were carried out at the R&D Centre for Telecommunications and Multimedia, part of the Institute for Systems and Computer Engineering, Technology and Science, located on the Campus of the Faculty of Engineering, Porto University.

The main purpose of the present work was to study the interactions of intensity-modulated laser beams with skeletal muscle and to test the possibility of reducing the light scattering and increase muscle transmittance through the creation of temporary optical clearing effects.

1.1 Contextualization

Lasers were first introduced into medical procedures 62 years ago, with their initial use in 1963 to treat human melanoma [1], [2]. Clinical diagnostic and treatment procedures have shown recent progress with increasingly less invasive and safer techniques for the patient. In 2023, there was a global investment of 128 billion dollars in clinical equipment based on optical technologies, which represents 73% of this market, while the investment in ionizing-related equipment was only 48 billion dollars. These values show the current trend to replace clinical equipment that is based on ionizing radiation with others that are based on optical technologies [3]. The replacement of ionizing radiation methods by optical-based methods leads to the minimization of the harmful effects that result from exposure to ionizing radiation, such as acute radiation sickness, multi-system syndromes, and genetic abnormalities at the cellular level [4].

The characteristics of lasers, such as the emission at a specific wavelength, the focusing of a thin, collimated beam, and coherence between photons, make them interesting for clinical procedures. Depending on the application, lasers can be broadly classified into surgical and non-surgical categories [5]. High-power lasers (>0.1 W) are typically used in diagnostic and

treatment procedures, such as Optical Coherence Tomography (OCT) [6], while low-power lasers (ranging from 0.001 W to 0.1 W) or light-emitting diodes (LEDs) are used in therapeutic contexts, such as in low-level laser therapy (LLLT) [7]. LLLT is known to promote wound healing by stimulating cell regeneration and enhancing blood flow in the injured tissue [8]. In that context, the use of lasers is very complex since, for each wavelength, the laser induces particular effects on tissues. Additionally, the effects of laser use in clinical procedures are determined by a combination of laser-tissue interaction, the selection of appropriate laser parameters, and more suitable delivery systems [9]. The diverse applicability of lasers in the field of Biophotonics was already demonstrated in areas such as cosmetics [10], general medicine [9], ophthalmology [11], and oral medicine [12], as it will be described with more detail in Chapter 2. The interest in using lasers to diagnose and remove tumors has also been increasing due to their ability to not damage adjacent tissue and cells, by inhibiting cancer cell growth and resulting in a reduction in the number of new cancer cases per year [13]. The advantages of using lasers in such applications include the use of non-ionizing radiation, shorter intervention times, minimal blood loss, and a lower risk of post-intervention infections [14].

Another advantage and unique capability of lasers is the ability to make very short pulses, which produce better results in clinical interventions, with fewer side effects than continuous emission lasers [15], [16], but lose efficiency at great depths within the tissues [17]. Such limitation of the efficiency of lasers at low tissue depths is caused by the strong light scattering properties that tissues present, mainly in the ultraviolet (UV) range [18], [19], [20], [21], [22]. Although UV light is cytotoxic, lasers emitting in this spectral range present some advantages, such as a higher frequency that allows carrying more diagnostic information, or greater efficiency in the photoablation of tumors, as long as low doses of radiation are used for a short time, leading to a reduced tissue exposure [23]. Given these advantages, recent investigations have focused on this spectral region, particularly regarding its application in the management of superficial corneal infections [24]. In this study, pulsed low-power UV light (λ= 265 nm, I= 1.93 mW/cm^2, f= 20 Hz) produced a more effective antimicrobial response in *ex vivo* corneal tissues compared to continuous irradiation under the same conditions. At the opposite end of the spectrum, non-invasive phototherapy using near-infrared (NIR) light at 810 nm has demonstrated the potential of transcranial photobiomodulation to modulate Alzheimer's disease pathology [25]. Continuous-wave stimulation primarily enhanced astrocyte activation and vascular remodeling, while 40 Hz pulsed stimulation facilitated microglial recruitment to β-amyloid plaques, promoting their clearance.

Tissue optical clearing is a technique that creates transparency in biological tissues, leading to an increase in the light penetration depth, which results in various benefits, such as improved imaging contrast and resolution from deeper layers of tissues [26]. This technique has been studied in various tissues, such as human colorectal mucosa (normal and with cancer) [27], lung [28], or skeletal muscle tissue [29]. In addition to the created transparency in these tissues, such studies produced innovative physiological and diagnostic results. In one of these studies, it was found that the applied clearing treatment led to the creation of high transparency windows located in the UV, between 200 and 300 nm [30], a spectral range where strong light scattering is associated with intense absorption bands of proteins and DNA [31]. As tumor tissues are known to have higher contents of proteins and DNA than the corresponding healthy tissues [32], [33], it is of great interest to study the attenuation of laser pulses in this spectral range and how the transparency effects minimize that attenuation. Additionally, UV lasers are interesting to study the protein dissociation in tissues that highly concentrated glycerol solutions induce [34] as a potential method to delay cancer progression. This information leads us to the motivation behind this work, which will be described in the next section.

1.2 Motivation

There is a concerted effort by clinical practice to minimize the exposure of patients to ionizing radiation, as well as the preference for non-invasive methods in clinical procedures. In this sense, it is clear that the recent research and development related to optical methods allowed to perform a great step forward in finding non-invasive or minimally invasive alternatives to ionizing methods that are currently standardized. Although further research is required for the fully replacement of ionizing procedures by optical methods, the use of tissue clearing techniques in conjunction with existing spectroscopic or imaging techniques has already helped to reach higher tissue probing depths and reach innovative diagnostic data.

Therefore, due to their characteristics and advantages, lasers are a promising option for in-depth diagnostic and treatment procedures and are already being used in some medical contexts. However, to develop innovative and less invasive clinical procedures, which are based on the use of lasers, it is crucial to study the interactions of intensity-modulated laser beams with tissues as a function of wavelength and how laser transmittance by tissues is improved by the creation of tissue transparency.

Moreover, the way light is delivered, particularly in pulsed mode, can significantly influence the light-tissue interaction procedures. This way, a better characterization and optimization of this form of delivery can enhance effectiveness while minimizing potential damage, further reinforcing the value of light-based technologies in the development of safer, more precise, and less invasive medical applications.

1.3 Objectives

By performing laser transmittance measurements from tissues, this work aims to characterize the attenuation of intensity-modulated laser beams as a function of wavelength. Using lasers emitting from the UV to the NIR, it will be possible to quantify and compare the scattering that the tissue produces in the beam in different areas of the spectrum.

A second objective of this work is to test the possibility of increasing the transmission of intensity-modulated laser beams through the creation of temporary and reversible transparency effects that are applied to reduce light scattering in the tissue samples. For that, four optical clearing agents were used: sucrose, glycerol, electronic cigarette (E-cig) fluid, and tartrazine (TZ). The first three are well-known and characterized optical clearing agents, and the last is a recently discovered agent that is currently under study by many research groups. The comparison between the transparency effects created by these agents in muscle tissue is one additional objective of the present work.

Overall, this study aims to produce results that will contribute to the optimization of current laser diagnostic and treatment techniques that are currently used in clinical practice, so that shorter intervention times, easier practices for the clinician, and higher comfort for the patient can be obtained.

1.4 Document structure

The present document is organized into five chapters. The first chapter provides the contextualization of the work, followed by the motivation and objectives that led to this research work. The second chapter describes the state of the art related to this work, focusing on the published literature related to applications of pulsed or intensity-modulated lasers and the tissue clearing method. In the following chapter, all the materials, methods, and calculations are described in detail so that this work can be replicated. The results obtained, as well as their

discussion, are presented in chapter 4. Finally, in chapter 5, the conclusions of this work are presented, as well as future perspectives for possible future studies that can add further innovative data.

Chapter 2 - State of the Art

2 State of the Art

2.1 Biomedical photonics

Biophotonics is a multidisciplinary life science that uses knowledge from physics, optics, and electrical engineering to study and manipulate biological systems. In the second half of the XX century, due to the availability of new instrumentation, like fiber optics and small-sized lasers with emission at various wavelengths, this research field gained high interest within the scientific community. Since then, several research groups have made diverse and highly important studies that provided various physiological and diagnostic data, new clinical methodologies and the improvement of others. In practical terms, current Biophotonics methods allow functional and structural characterization of different types of cells and tissues with high resolution and contrast [35].

This type of characterization has allowed a better understanding of the cells and their structures, a knowledge which, until then was obtained mainly through histological and imaging techniques, such as computed tomography (CT) and magnetic resonance imaging (MRI). CT allows precise imaging of subcellular structures, however, in the context of thick tissue samples, this technique lacks spatial context. In contrast, MRI has limited resolution, not allowing to differentiate individual cells. Additionally, the histological and imaging techniques, such as CT, have the disadvantages of being invasive and having long-term carcinogenic effects [36], [37].

These questions and limitations have been solved in the last years, with the emergence and development of optical imaging techniques within the field of Biophotonics. The use of light to study biological structures is not recent, it all started in the XVII century, with the invention of the microscope [38]. Until the second half of the XX century, the knowledge that light could be used in a diagnostic or therapeutic context already existed, but the lack of technology did not allow optical techniques to evolve [39].

When applied to diagnostic and treatment procedures, Biophotonics methods have the main advantage of being non-invasive or minimally invasive, which is in line with the current trends of replacing medical techniques and equipment by non-invasive alternatives. Some examples of non-invasive Biophotonics methods are the different types of optical spectroscopy techniques, such as optical spectroscopy, Terahertz (THz) spectroscopy, fluorescence spectroscopy, and Raman spectroscopy. Zhou *et al*. have showed that Raman spectroscopy was

able to discriminate between normal, cancerous and benign lesions of brain tissue, through the differences in amplitude and shape of the spectra characteristic of the different conditions [40]. Deo *et al*. have proven that fluorescence spectroscopy combined with machine learning can detect cervical cancer at earlier stages more efficiently than current diagnostic methods [41]. Regarding THz spectroscopy, it is one of the most recent techniques in the field of Biophotonics, with a particular sensitivity to tissue water content. That characteristic allows the differentiation between normal and cancerous tissues and has already been used to identify skin, breast, and brain cancer *in vitro* and *in vivo* [42]. In addition to diagnostic techniques by spectroscopy methods, different optical imaging modalities are also widely used to perform diagnostics. Considering the imaging methods, some examples are Raman imaging, OCT imaging, Second Harmonic Generation (SHG) imaging, and Speckle imaging, among others [35]. In 2022, Schwartz *et al*. proposed a model that combines machine learning with OCT for the identification of ovarian cancer in mice [43]. *Hase et al*. have shown that SHG imaging can be used to monitor the tendon healing process, due to its capacity to reflect the structural maturity of collagen molecules and their aggregates, without the need for histological sectioning [44]. In terms of Speckle imaging, Qureshi *et al.* developed an optical speckle image velocimetry, which uses particle image velocimetry combined with speckle physics to measure the quantitative blood flow [45]. Finally, there is a last group of techniques that uses laser beams and are also minimally invasive and highly promising, which will be discussed in more detail in the next section.

2.2 Lasers

As previously mentioned in the Introduction, the invention of the laser is not recent. In fact, it was in 1960 that Theodore Maiman created the first human-made laser by pumping a synthetic ruby rod with a flash lamp. In physical terms, the laser beam results from the excitation of atoms in a gas, liquid, or crystal medium to obtain stimulated emitted photons from these media. As the excitation photon energy propagates through the medium, bouncing between two mirrors, it causes the excitation of atoms, which, when decaying to the fundamental energy state, will release additional photons that will join the excitation process, producing a gain energy that eventually results in a high-power beam of light that can exit the laser cavity through one of the mirrors that is semi-transparent. Since their discovery, various types of lasers have been developed, as well as the fields in which they have been applied.

Nevertheless, the use of laser technology in biology, and in particular in clinical applications, remains one of its most impactful and widely adopted applications [15]. The use of lasers in Biophotonics research requires that the properties of both the laser and the tissue should be known. In the case of tissues, their broadband spectral optical properties, along with internal composition, component concentrations, thermal conductivity, or even heat capacity should be studied [46]. Regarding lasers, the emission waveform (continuous or pulsed), wavelength, and power are also very relevant to conduct research.

Laser pulses concern light emission by lasers with limited time duration, which is repeated over time. The time duration for a single laser pulse is in general in the range from femtoseconds to nanoseconds, and depending on the desired pulse duration, energy, repetition rate, and wavelength, various pulse generation techniques and distinct types of pulsed lasers are employed [15], [47]. To generate pulses with durations on the order of nanoseconds and a pulse repetition between 10 Hz and 100 kHz, Q-switched lasers, typically solid-state bulk lasers, are commonly employed. These systems are capable of producing high-energy pulses, often reaching the millijoule or even multi-joule region. Moving on to pulses with a duration in the order of picoseconds or femtoseconds, these are usually generated with mode-locked lasers, which can be solid-state lasers, fiber lasers, or semiconductor lasers. This type of pulses have a repetition rate, normally, between 50 MHz and a few gigahertz and a pulse energy quite small [47], [48].

Given the wide variety of pulse types and their highly configurable nature, there is a great interest in developing new clinical applications that use pulsed lasers because such lasers can penetrate deeply into tissues without thermal damage, as it is verified when using lasers in continuous emission modality. Pulsed lasers also allow probe cooling between pulses, which controls beam directionality and tissue ablation [49].

Laser lithotripsy is a good example of clinical applications of pulsed lasers. In this technique, photomechanical or photothermal effects are used to fragment biliary or urinary stones, in a minimally invasive manner [50]. Pulsed lasers have also been used to treat neuronal tumors [51], or in photodynamic therapy procedures to treat lung cancer lesions [52]. Colorectal tumors have been resected with high precision, using infrared ultrafast pulsed lasers, without damage to the surrounding tissues [53]. Pulsed lasers are also used in the treatment of post-mastectomy pain syndrome [54], or in the MRI-guided laser-induced thermal therapy [55], a procedure that allows the treatment of epilepsy through the implantation of a pulsed diode laser in the brain. NIR pulsed lasers can also be a great support to patients suffering from skeletal muscle

pathologies, allowing the reduction of pain and inflammation, or even to stimulate healing [49], [56]. Finally, in the case of post-dermatological surgical scars, pulsed dye lasers are also of great interest in minimizing scar visibility [57]. All these and other surgical techniques have been applied based on the experience and senses of the medical professionals, and in some cases by slicing the upper layers of tissue to reach deeper for tumor ablation. Such fact shows that higher precision and better treatment efficiency could be achieved if knowledge regarding the pulse attenuation and its minimization through induced transparency would become available. The pulse attenuation is created both by light absorption and light scattering inside the tissue, leading to a reduced light penetration depth [46]. As an example, in photocoagulation and photoablative interventions, targeting areas at significant tissue depths becomes challenging [17]. The combination of such procedures with optical clearing (OC) treatments leads to an improved laser beam at greater tissue depths. The OC treatments have been widely studied in various human and animal tissues, where agents such as glucose, E-cig fluid, glycerol, and many others were used as optical clearing agents [27], [28], [34]. The created transparency effects are reversible and present no side effects, making them adequate to use with pulsed laser procedures. Given the relevance of the OC method to the field of Biophotonics, the following sections will present further information about this method, the mechanisms that lead to tissue transparency and the possible applications.

Similar to laser pulses, intensity-modulated laser beams can benefit from the use of OC techniques. Intensity-modulated and pulsed laser beams present some similarities, since the emitted energy is restricted to time intervals. However, the key difference is that a modulated laser simply switches on and off at regular intervals, operating at a fixed maximum output power whenever it is on, regardless of how quickly or slowly the modulation occurs. The application of intensity-modulated laser systems in a clinical context has shown diverse and significant benefits across surgical, imaging, and therapeutic contexts. In 2006, Geldi *et al*., studied the effect of a modulated vs continuous wave surgical diode laser system on *in vitro* lamb liver tissue [58]. A 980 nm diode laser was used and the modulated mode (20 Hz) produced significantly better outcomes than the continuous mode, achieving larger coagulated tissue areas with minimal carbonization. Specifically, while continuous mode operation at 16 J resulted in a carbonized area, with a thermally altered area ratio of 0.35, the modulated mode achieved a much lower ratio of 0.05 even when delivering 160 J (ten times more energy). These findings highlight the critical role of modulation in improving surgical laser safety and efficiency. Relative to imaging application, Maslov and Wang, developed a photoacoustic imaging system

using a continuous-wave laser source, which was intensity-modulated [59]. They used a 784 nm laser, with 120 mW of power modulated at 2.45 MHz. Despite its lower power compared to pulsed lasers, this intensity-modulated setup achieved good lateral (450 μm) and axial (1 mm) resolution in imaging biological tissues, including vasculature in rabbit ears and legs. Finally, in the therapeutic context, Baratto *et all*, investigated a very low-power modulated laser at 635 nm for therapeutic use in osteoarthritic patients [60]. Despite power levels as low as 0.3 mW, the modulated application (rectangular waveform at 500 Hz) induced measurable changes in soft tissue thickness, assessed via ultrasound, with no significant thermal effects, indicating a likely non-thermal, tissue-excitability mechanism.

2.3 Light scattering in tissues and ways to reduce it

The phenomenon of tissue transparency is not new, as it is already present in nature, more precisely, in a significant number of animals, such as cephalopod, gelfish, mollusks, zebrafish larvae, some butterflies and insects, that use transparency mechanisms to defend themselves from predators and survive [61]. Apart from these specific animals that exhibit transparency in their natural form or that can adapt to create temporary transparency, the majority of living beings, including humans, are composed of biological tissues that are opaque to light. Microscopically speaking, the tissues are not homogeneous, being composed of a combination of proteins, carbohydrates, lipids, blood, and higher-sized structures, permeated by the interstitial fluid (ISF), which is mainly composed by water (>90% of its volume) [35]. Therefore, since water has a low refractive index (RI) when compared to the other tissue components, a RI mismatch between the ISF and the other components occurs [26].

Considering a light beam propagating inside a tissue, its intensity and collimation will be decreased by the optical properties of the tissue. By one side, photons in the beam with wavelengths coinciding or within the absorption bands of tissue components will be absorbed by those components. By another side, mainly due to the RI mismatch between tissue components that was described above, photons will be scattered from their original propagation path. Considering the absorption of photons, the absorption coefficient (μ_a) of a tissue represents the number of photons that are absorbed per unit path length within the tissue, which is generally represented in cm^{-1}. On the other hand, the scattering coefficient (μ_s) of a tissue, also commonly represented in cm^{-1}, represents the number of photons that are scattered per unit path length inside the tissue. Both these optical properties are wavelength-

dependent and the combination of the absorption and scattering phenomena is usually designated by attenuation, where the attenuation coefficient (μ_t) of the tissue is calculated as the sum of μ_a with μ_s [26]. Most of biological tissues present strong scattering properties, always higher than absorption in the UV-NIR spectral range, and such relation tends to increase with decreasing wavelength [21]. There are other optical properties that are used to characterize biological materials, such as the scattering anisotropy factor (*g*), which measures the directionality of scattering, or the light penetration depth (δ), which measures the depth inside a tissue where the intensity of a light beam is reduced to 37% of the intensity introduced at the surface [26].

The strong light scattering that occurs in tissues is the main obstacle for the application of light-based technologies in deep-tissue diagnostics and treatment procedures [19]. Such scattering occurs due to two mechanisms. The first one is that photons are scattered when colliding with certain tissue components, and the second is originated by the RI mismatch between the ISF and the other tissue components when considering the Snell-Descartes law of refraction. As referred above, the water volume content in the ISF is higher than 90%, which imposes a low RI to the ISF, due to the low RI of water, which is 1.33 at 589 nm [26]. This RI is considerably low when compared to the RI of the other tissue components [26], [62]. As an example, skeletal muscle is a fibrous tissue that contains long dielectric cylinders (actin and myosin fibers), which are grouped in fiber cords with an average diameter of 53 μm and RI=1.53 at 589.6 nm. These fiber cords are permeated by the ISF that has a RI = 1.35 to 1.37 at the same wavelength [26]. Considering a possible refraction from the ISF into the fiber cords of the muscle, such RI mismatch leads to light scattering, preventing the use of light beams at significant tissue depths. Since each tissue component has distinct optical properties, the overall optical properties of a tissue that result from experimental measurements, are a weighted average of the optical properties of all tissue components, and do not allow to quantify such local RI discrepancies directly [26].

Due to this strong light scattering that occurs inside biological tissues, the ability of light to penetrate the tissue is affected, limiting the application of optical methods in the clinical field, when it is necessary to reach considerable depths. To overcome this problem and allow light beams to reach deeper in tissues, various methods were tested and studied. In this sense, the tissue whitening method, the tissue compression and stretching method, and the immersion method have emerged in the late XX century [26]. The first method is based on the use of some agents, such as acetic acid, to induce tissue turbidity and consequently increase the contrast in

images that are acquired from tissues. The second method relies on the application of mechanical forces, such as stretching and compression, which lead to an increase in tissue optical homogeneity through the removal of the tissue fluids. Both methods have advantages and limitations, which forced researchers to look for better alternatives. Such better alternative is the optical immersion method, which was first discovered by in the beginning of the XX century by Werner Spalteholz, a Germain anatomist [35]. In 1911 and 1914, Spalteholz published two papers reporting the use of organic solvents to induce transparency in large tissue samples. Although he could understand that a mechanism of RI matching between tissue components is at the basis of the creation of tissue transparency [26], the fully explanation for the tissue transparency and its mechanisms was only given at the end of the XX century, in a paper published by Tuchin *et al.* [63]. This method has the great advantage of being reversible, increasing its application possibilities, including *in vivo*. Considering the various advantages of the optical immersion method, and since it represents part of the research presented in this work, the following two sections present more detailed information about this method.

2.4 Optical clearing method

As previously mentioned, the purpose of creating transparency in tissues is to minimize the light scattering inside and increase the light penetration depth for diagnostic and treatment purposes. Considering the tissue immersion method, such transparency can only be achieved through the total or partial replacement of tissue water by an agent, commonly designated as optical clearing agent (OCA) [64]. In the last decades, an increasing number of research studies has been done to characterize the optical clearing mechanisms, evaluate the transparency efficiency and discover new OCAs. One result of these studies is that a wide range of different substances has proved to be useful to increase tissue transparency. Overall, the OCAs can be classified into five groups: the group of sugars (e.g., glucose, fructose, and sucrose); the group of organic acids (e.g., oleic and linoleic acids); the group of alcohols (e.g., glycerol, polyethylene glycol, and polypropylene glycol); the group of contrast agents (e.g., Verografin™, Trazograph™, Hypaque™, and Omnipaque™) and the group of other organic solvents such as thiazone and dimethyl sulphoxide [65]. The most used OCAs are glucose, glycerol, and polyethylene glycol due to their biocompatibility and nontoxicity effects in tissue samples. Nevertheless, it is crucial to find an optimal agent and the safest concentration for application on living tissues, since each agent interacts differently with the tissues and varying concentrations of the same agent can

also produce different transparency effects. All of the OCAs previously mentioned have already been successfully used in the optical immersion method to improve Biophotonics methods [65].

In addition to a good biocompatibility to tissues, OCAs should have a high RI when compared to water, so that by increasing the mean RI of the ISF and/or sarcoplasm, a RI matching between these fluids and the other tissue or cell components, which are commonly designated as tissue scatters, is obtained [64]. As previously indicated for the case of the skeletal muscle, the muscle fibers present a RI of 1.53 at 589 nm and the ISF that permeates the fibers has a mean RI between 1.35 and 1.37. By replacing the interstitial water in the muscle, even in a partial manner, by an OCA, such as glycerol, with a RI of 1.47 [66], the mean RI of the ISF will approximate the RI of the muscle fibers, leading to a decrease in light scattering in the muscle [64].

To understand the OC method in more detail, we have to take into account that, according to literature, the biological tissues have four stages of water that result from their binding strength: free water, weakly bound, tightly bound, and strongly bound [67], [68]. The first two binding-states of water can move freely to the outside when stimulated by the osmotic pressure of an OCA and together are commonly designated as mobile water. The tightly bound and strongly bound water, which are commonly designated as bound water, are responsible for maintaining the hydration of tissue and cell components. Such bound water can be converted into mobile water, provided that the tissue is immersed in a highly-concentrated OCA solution for several hours or even days [64].

Considering all these aspects, when a tissue sample is immersed in a solution with a particular OCA concentration, some mechanisms that lead to the creation of transparency will occur. At the beginning of the immersion, the osmotic pressure of the OCA in the solution where the tissue sample is immersed will force the mobile water in the ISF to flow out from the sample. Such water loss to the outside will originate a decrease in sample thickness, which is accompanied by the approximation of the tissue scatterers that rearrange themselves in a more organized and compacted way in a small volume. Such effect can also be obtained through the application of stretching or compression mechanical forces, but the tissue immersion technique is reversible in a fast manner and does not leave side effects [35]. Such compact organization of tissue scatterers leads to the increase of scatterer density, which results in an increase of μ_s. However, the improved and compact organization of the scatterers and the decrease of sample thickness lead to a better forward scattering of light and to an increased sample transparency. This mechanism, designated as tissue dehydration, is one of the three main mechanisms in the

OC immersion method that contributes to increase tissue transparency. As the mobile water begins to move out due to the osmotic pressure created by the OCA molecules in the treating solution, it becomes easier for the OCA molecules to diffuse into the tissue. This diffusion can take several minutes until saturation is reached, but during the first few minutes of the treatment, both fluxes (OCA flowing in and water flowing out) occur simultaneously. Once saturation is reached, the OCA flux into the tissue ends and the OCA molecules that have infiltrated and occupied all the interstitial spaces within the tissue lead to the increase of the global RI of the ISF, approaching it to the RI of the tissue scatterers. This is the basis of the RI matching mechanism of the OC immersion method. As a result of such RI matching between tissue fluids and scatterers, light scattering inside decreases, leading to an artificial, temporary and reversible transparency in the tissue that allows light to reach higher tissue depths. The tissue dehydration mechanism is also reversible and such reversibility can be obtained by immersing the treated *ex vivo* samples in saline for a few minutes, as previously demonstrated [28]. For *in vivo* tissues, the reversibility of the dehydration and RI matching mechanisms occurs naturally, since the mobile water from the adjacent tissues will force the OCA molecules to move out, which will later be expelled through the urinary system [64]. In some cases, when the OC immersion method is applied to treat tissues with highly concentrated solutions of hyperosmotic OCAs, such as glycerol or some sugars, a third OC mechanism also occurs. When the concentration of OCA molecules in the interstitial locations becomes high, those molecules begin to interact with the proteins in the tissue scatterers, inducing their dissociation. Since proteins present their absorption bands in the deep-UV [31], [69], the destabilization and dissociation of protein chain connections leads to a decrease in the magnitude of the absorption bands, which combined with the decrease of light scattering originates an increase in transparency in the UV range [34], [35]. Such mechanism is also reversible through the replacement of the OCA molecules by saline solution, as previously verified using different techniques such as SHG imaging and Raman spectroscopy techniques [70], [71], [72].

2.5 The evolution of optical clearing techniques and their applications

The application of optical clearing techniques is not a recent development, with the earliest evidence of their use tracing back to ancient times. The early inhabitants of north America and north Europe unconsciously used dried animal skin to construct the walls of their

dwellings or dehydrated seal intestines for windows, in order to allow the light to enter. However, scientific evidence of transparency techniques only emerged at the beginning of the 20th century, with two publications from Werner Spalteholz in 1911 and 1914 [73], [74]. Spalteholz was a German anatomist who observed that by sequentially immersing muscle tissue in alcohol, clove oil or xylene and finally in Canadian balsam, increased tissue transparency. Additionally, Spalteholz also understood the occurrence of the RI matching mechanism and associated it with the transparency phenomenon. Since then, due to no utility of such discovery, the research in the field of tissue clearing was forgotten and only resumed in the second half of the XX century. It was in the late 1980s and early 1990s that this technology began to be intentionally developed to address the challenges faced by the rapidly advancing optical methods in clinical diagnostics and therapy, more precisely, with the appearance of lasers and light diodes [20].

Later in 1997, Valery Tuchin and his group at Saratov State University (Russian federation), published the first article that describes the propagation of light in tissue with controlled optical properties [63]. In this article, they evaluated the optical properties of the sclera before and after transparency treatments with Trazograph^{TM}, glucose, and polyethylene glycol. As a result, they found that treatment with OCAs causes a reduction in light scattering in the tissue and a consequent increase in transparency. This discovery, as well as the mathematical formalism of OCA diffusion in tissues through the Fick's laws of diffusion, has triggered research efforts worldwide, reigniting interest in the field.

Since then, much research has been done relative to the OC immersion method, its combination with optical diagnostic and treatment techniques, and the testing of new OCAs. The OC method has been used in several applications, one of them being the evaluation of the diffusion properties of different OCA molecules in various tissues. Pinheiro *et al.* used collimated transmittance (T_c) and diffuse reflectance measurements to obtain the diffusion time and the diffusion coefficient values that characterize the unique water and sucrose fluxes in the muscle [29]. This approach can also be used to differentiate the diffusion properties of agents between healthy and diseased tissues, especially in cases of cancer and diabetes mellitus. Carvalho *et al*. investigated the diffusion properties of glucose and water in healthy and cancerous colorectal mucosa [27]. As a result, they verified that glucose diffusion was slower in cancerous tissues, with measured diffusion times of 320.6 ± 10.6 s compared to 299.2 ± 4.7 s in healthy tissues, and also that cancerous tissues exhibited a higher mobile water content (64.4%) than healthy mucosa (59.4%). Tuchina *et al.* estimated the glucose diffusion coefficients in *ex*

vivo mouse skin, comparing tissues from diabetic mice (alloxan induced diabetes) to those from non-diabetic mice [75]. As a result, diabetic skin showed 1.5 times higher optical clearing efficiency, but glucose diffusivity was 2 times slower compared to non-diabetic skin. The reversibility of the OC immersion method has also been proven, when Oliveira *et al*. measured the spectral T_c of lung tissues treated with E-cig fluid, followed by immersion in saline solution, to assess the reversibility of the treatments [28]. The immersion in saline solution effectively reverted the clearing effect across the 220–1000 nm spectral range. Curiously, in this study, after reverting the transparency, a second treatment with E-cig fluid produced a transparency with almost doubled magnitude, when compared with the first treatment, suggesting that the initial treatment may have converted some bound water into mobile water, enhancing the subsequent clearing effect.

Even with all these advances, there are still several challenges to overcome in the field of tissue clearing. The difficulty of using OC techniques *in vivo* is one of them, since the internal fluxes of water between adjacent tissues limits the OC potential in terms of applicability. However, in recent years, several steps have been taken towards the application of OC treatments *in vivo*. Zaytsev *et al.* used the OC method combined with physical and chemical methodologies to enhance skin permeability to OCAs to determine the clearing-effectiveness of biocompatible OCAs using line-field confocal optical coherence tomography imaging [76]. In this study, several mixtures of OCAs were used and all of them have increased image intensity and contrast, with the best performance achieved using a mixture of polyethylene glycol, oleic acid, and propylene glycol. The developed OCAs, compliant with drug safety standards, significantly improved skin transparency, allowing deeper and higher-contrast imaging and enhancing line-field confocal optical coherence tomography diagnostic capabilities [76]. Franzesi *et al.*, by superfusing the brain with small amounts of biocompatible, RI–raising materials, achieved several-fold signal improvements under one-photon and two-photon microscopy, enabling visualization of previously undetectable cells [77]. It was observed in that study that enhancements were consistent across different fluorescent wavelengths, and crucially, neuronal functional properties remained unchanged in both awake imaging and *ex vivo* assessments. Banerjee *et al*. used an oil-based OCA to enhance data quality in optical coherence tomography angiography [78]. *In vivo* tests on mice and humans showed effective optical clearing of tissues, which was translated in a better contrast of the OCT images. Computational analysis revealed that, compared to controls, the application of the OCA significantly improved vessel visibility and vascular signal intensity with depth.

Important steps have also been taken towards the discovery of new OCAs. Recently, Ou *et al.* used TZ, a yellow food dye, to create a temporary transparency effect on the skin of live rodents [79]. In this study, applying the Lorentz oscillator model, it was observed that TZ is able to significantly increase the RI of tissues for longer wavelengths than the one where its absorption band occurs – 428 nm. The highly promising results obtained have generated a great deal of interest from the scientific community in general, but more studies are needed to validate this new OCA and to approve its application in creating transparency, since TZ is considered the most allergenic of all the azo dyes and is particularly liable to cause reactions in asthmatics and individuals with aspirin intolerance [80], [81], [82]. TZ is also a fluorescent dye, especially when in high concentration, meaning that fluorescent imaging methods should be carefully applied when TZ is used to create transparency in tissues. To study further the potential side effects of TZ in tissues, Thanh *et al*. verified that TZ causes vascular disruption in developing zebrafish embryos *in vivo* and on human umbilical vein endothelial cells *in vitro* [83]. These results raise some questions about the biocompatibility of the TZ and the impact it may have on humans.

Finally, one field of research that could benefit from the use of OC method is the laser field. Within the scientific community, few articles describe the combination of tissue transparency with laser methods in clinical practice. Ma *et al.*, in their study, provided an improved treatment of port-wine stains, which often respond poorly to pulsed dye lasers, by using multiple laser pulses from a 1064 nm Nd:YAG laser combined with glycerol application [84]. The goal of this study was to reduce the laser energy required for effective blood coagulation in vessels, so that minimized damage to surrounding tissues could be achieved. As a result, the application of anhydrous glycerol significantly enhanced optical clearing, with a 36.69% decrease in diffuse reflection and a 38.73% increase in transmission at 1064 nm. This led to a 25% reduction in the number of laser pulses needed for coagulation and a 35% decrease in incident energy. In both *in vitro* (capillary tube model) and *in vivo* (hamster dorsal skin) experiments, glycerol application reduced the number of pulses needed to achieve vessel blockage, showing improved efficiency in treating deeper or larger capillary vessels while minimizing thermal damage to normal tissue [84]. More recently, Shariati *et al.* developed a combined clearing approach, which integrates three techniques—agent-based clearing, ultrasound-induced optical waveguides, and temporal optical clearing—to significantly enhance light penetration depth in biological tissues [85]. By combining these three methods, the researchers achieved a 10-fold increase in light penetration depth in chicken breast tissue (from

0.67 cm to 6.7 cm), setting a new record in the field. Light transmission improvements were validated using OCT, T_c measurements, and fluorescence tests. In the T_c tests, they measured the light intensity before and after passing through the tissue to calculate the effective attenuation coefficient, before and after tissue clearing, through the Bouguer-Beer-Lambert law, using a nanosecond diode laser and a femtosecond Ti:Sapphire laser, both emitting at 800 nm. By obtaining a reduction of the attenuation coefficient as a result of the clearing procedures, this work represents a major advancement toward safer, faster, and more effective optical imaging techniques, applicable from cellular to organ-level diagnostics [85].

A similar approach, using laser modulated transmittance measurements, will be used in this work, when studying skeletal muscle samples. The main objectives of this work are to characterize the attenuation of intensity-modulated laser beams as a function of wavelength and to study how muscle transmittance at those laser wavelengths improves with OC. The obtained results are intended to add valuable information that can be used in the future to develop innovative and less invasive clinical procedures centered on the use of lasers.

Chapter 3 – Materials and Methods

3 Materials and Methods

3.1 Sample preparation

As previously mentioned, the tissue selected to conduct this study was the skeletal muscle from rabbit, since it is similar to the human muscle, it is easy to obtain and has already been widely studied by the scientific community. Additionally, this animal, the European rabbit (*Oryctolagus cuniculus*), possesses a significant amount of muscle mass, making it suitable to collect a large number of samples for carrying out the number of measurements required for this study. It is important to mention that all experimental protocols involving the animals and tissue collection for research purposes were conducted in accordance with the principles outlined in the Declaration of Helsinki and were approved by the Ethics Committee of the Institute for Systems and Computer Engineering, Technology and Science, as documented in the official approval issued on July 6, 2023.

To obtain the samples to use in this work, a request for one animal was made to a local rabbit breeder. All the rabbit parts were used for research purposes, resulting in no waste of any kind. After animal sacrifice, the rabbit was then transported to the laboratory, where the measurements would be carried out. The carcass of the animal was kept frozen at a temperature of -20°C during the period of this research.

Whenever tissue samples were required for the experimental measurements, the rabbit carcass was retrieved from the low temperature storage, and a cuboid fragment with approximate dimensions of $2 \times 1 \times 1$ cm^3 was excised using a scalpel. The extracted fragment was then placed on a sample holder for insertion into a cryostat-microtome (Leica^{TM}, model CM1860 UV, Germany) for sample preparation. In the early stage, the sample holder was placed onto a rapid freezing platform located inside the cryostat-microtome. This platform typically maintains a lower temperature than the chamber of the cryostat-microtome, allowing the desired freezing temperature to be reached more quickly. Additionally, the temperature of the chamber was set to -7 °C, since this temperature is optimal for producing a uniform cut through the entire sample, allowing high-quality histological sections. To enhance the adhesion of the sample to the support platform, a small volume of saline solution was applied to its base using a syringe. Upon freezing, the saline acted as a bonding medium, securing the fragment firmly to the platform.

After approximately ten minutes, once the muscle fragment was properly secured to the platform and at the right temperature, it was ready to be sectioned. The platform containing the fragment was then placed on the cutting stage. Before initiating the actual sectioning, it was necessary to level the upper surface of the fragment to ensure clean and accurate cuts. With the cryostat-microtome set to produce 10 µm sections (minimum thickness allowed by this equipment), the surface was trimmed using consecutive cuts at this thickness to avoid unnecessary tissue loss. Once the surface of the tissue fragment was adequately leveled, sectioning of the sample was carried out. With the cutting stage calibrated to advance in 50 µm increments, ten successive advances were performed toward the blade, resulting in a total section thickness of 500 µm. The cryostat-microtome allows for precise adjustment of the cutting increments between 1 and 100 µm, which facilitates accurate and controlled sectioning.

Between two consecutive cuts, the tissue fragment was cleaned using a brush, and the surface was re-leveled as needed. Once the tissue sample was no longer usable or fully consumed, the previously outlined steps were carried out again to prepare an additional fragment. It is important to note that the chamber of the cryostat-microtome was kept closed whenever the tissue was not being handled, in order to maintain a stable internal temperature, as the ambient temperature in the laboratory was 20°C. Additionally, proper care was taken with the cutting blade, including covering it with its protective guard whenever sectioning was not being performed.

As the cuts were made, each tissue section obtained was placed on a microscope slide and immersed in saline solution to help thaw and promote the rehydration of the tissue so that it returns to its natural state. Each muscle slice remained immersed in saline solution for approximately 10 minutes before being used in the experimental procedures. Excess saline solution was carefully removed before the experimental measurements to prevent interference with the treatment process. Figure 1 shows some tissue samples immediately after sectioning, already immersed in the saline solution.

Figure 1 - Tissue samples immersed in saline solution.

3.2 Preparation of OCA solutions

The OC treatments that were applied to the tissue samples were conducted using four different OCAs: sucrose, glycerol, E-cig, and TZ. Both glycerol and E-cig agents were used in their pure form, that is, at a concentration of 99% for glycerol and as a glycerol/propylene glycol combination in the proportions of 70%/30% for E-cig. The other two agents were used in high-concentration aqueous solutions, 55% for TZ and 64% for sucrose. High-concentration solutions of sucrose and TZ were selected with the objective of producing the highest possible transparency effect in the muscle samples. It should be mentioned that although it was possible to prepare TZ solutions with higher concentration, the solution with 55% concentration was prepared, since it remains stable for a long period that is adequate for the study. Higher concentrated TZ solutions begin to precipitate TZ granules after approximately 40 min [86]. The following sections will provide a detailed description of the adopted protocol for the preparation of the solutions used in this work.

3.2.1 Glycerol and E-cig solutions

The glycerol solution (HidroDipro Laboratory, Portugal) used in the present study was acquired from a local store, in 100 mL bottles. Once purchased, its RI was measured at the laboratory and it was confirmed to have 99% purity. Such measurement was made at 589 nm and 20°C, using an Abbe refractometer (Kern^{TM}, model ORT-1, Germany). The E-cig was acquired from an online tobacco products retailer. Both glycerol and E-cig are transparent liquids at an ambient temperature of 20°C, and their concentrations are considered adequate for the research purposes, meaning that they are ready to be used in their pure state.

3.2.2 Sucrose solution

Sucrose grains are commonly used as sweeteners in food and beverages, and consequently can be acquired from any local store. Purchasing 1 kg of this sugar, it was only necessary to dissolve it in distilled water to prepare a solution with a desirable concentration. Since it was intended for this study to prepare a solution with a volume concentration of 64% of sucrose, it was initially required to calculate the RI for such solution. For this purpose, a reference database available at www.refractometer.pl was consulted, which provides RI values for sucrose solutions with concentrations ranging from 0% to 84% measured at a temperature

of 20°C. Collecting from this database the RI values for glucose solutions with concentrations of 10%, 20%, 30%, 40%, 50%, 60%, 70% and 80%, the curve fitting tool (CFTOOL) application in MATLAB™, was used to fit and interpolate such data. From this interpolation, it was observed that the dependence between the RI and the sucrose concentration in solution is not linear, and is described as a second-degree polynomial as follows, which was obtained with R^2=1:

$$n_{\text{sucrose}} = 7.708 \times 10^{-6} \times C^2 + 0.001342 \times C + 1.334, \quad (1)$$

where $n_{sucrose}$ is the RI of the sucrose solution and C is the concentration of the same solution, represented in percentage.

Since we wanted to use a solution containing 64% of glucose, the RI of that solution at 20°C was calculated with Eq. 1, obtaining 1.4514. After obtaining this RI value, the solution was prepared by dissolving sucrose grains in distilled water. To accelerate the dissolution of the sucrose grains, ultrasound was used over the solution recipient, which was inserted in a water bath (Geti GUC 02A, Opava, Czech Republic) at 30°C. Once the solution was fully homogenized, it was removed from the water bath and allowed to cool naturally until reaching the ambient temperature of 20°C. Once this temperature was reached, the RI of the solution was measured with the Abbe refractometer. If the RI was lower than 1.4514, additional sucrose was added to the solution, and if the RI was higher than this value, some drops of water were added to decrease the RI of the solution. All the procedures in this preparation were repeated until the desired RI value was measured from the solution. As a final verification, the solution was inspected visually to ensure that no sucrose granules have adhered to the recipient walls or deposited at the bottom.

3.2.3 Tartrazine solution

The TZ powder used to prepare the solution for the OC treatments was obtained from a local food dye supplier (Food Colors, www.corante.pt, Valongo, Portugal). Since TZ is a new OCA with limited information available, it was first necessary to perform some calculations to find the necessary mass of TZ powder that needs to be dissolved in a volume of water so that a desired volume concentration of TZ in solution is obtained. We describe such calculations in detail in our recent paper [86], but the essential steps to prepare a solution that contains 55% of TZ are described next.

The first step to prepare TZ solutions was to evaluate the bulk density (ρ_{TZ}) of the TZ powder. Measuring both the mass and volume of various TZ powder samples, it was possible to obtain ρ_{TZ} as 0.59 g/mL. Selecting a total solution volume of 25 mL, and considering that the desired solution should have a volume concentration for TZ of 55%, the volume of TZ (V_{TZ}) to be dissolved in water should be 13.75 mL, as calculated through Eq. (2).

$$\%\frac{V}{V} = \frac{V_{\text{solute}}}{V_{\text{solution}}} \times 100 \;\leftrightarrow\; 0.55 = \frac{V_{\text{TZ}}}{25} \;\leftrightarrow\; V_{\text{TZ}} = 13.75\ \text{mL} \tag{2}$$

After obtaining the value for V_{TZ} that is required to prepare the solution, the mass of the TZ powder can be calculated through ρ_{TZ} as follows:

$$\rho_{\text{TZ}} = \frac{m}{v} \;\leftrightarrow\; 0.59 = \frac{m}{13.75} \;\leftrightarrow\; m = 8.113\ \text{g} \tag{3}$$

Knowing the required mass of TZ powder (m = 8.113 *g*) to prepare the desired solution and the volume of water (25 – 13.75 = 11.25 mL) to mix, the preparation of the 55%-TZ solution was initiated. First of all, it was ensured that the ambient temperature in the laboratory was fixed at 20°C. With all the necessary conditions guaranteed, 8.113 g of TZ powder was weighed in a precision weight scale (Muvip, model MV0257, China). During mass measurements with the scale, this amount of TZ powder was already inside a glass container, whose mass was subtracted from the actual measurements. The 11.25 mL of distilled water were delivered into the glass container with a graduated syringe, and the mixing was made with the help of ultrasound, when immersing the glass container in a water bath at 30°C. This heating was done to accelerate the dissolution of TZ in water and obtain a uniform solution. After preparing the mixture, and performing a visual inspection to guarantee that no TZ granules were observed inside the glass container, the solution was cooled down to 20°C, and its RI was measured with the Abbe refractometer. This measurement resulted in a RI of 1.4326, which matched the calculations made in our recent paper [86]. Since this solution remains stable to use only for 45 min, prior to using it to create transparency in muscle samples, its RI was measured once again and possible mixing corrections were adopted to guarantee a uniform solution containing exactly 55% of TZ.

3.3 Experimental measurement setups and procedures

Although this research was conducted for several days, in each day once the tissue samples were prepared and the solutions ready, the experimental measurements could then be initiated. In this study, two distinct experimental setups and procedures were employed to acquire the data required for subsequent analysis and result extraction. Both experimental setups and their corresponding procedures are described in detail in the following subsections.

3.3.1 Collimated transmittance and absorbance measurements

The attenuation experienced by light as it passes through the tissue is governed by the optical properties of the tissue [26]. Consequently, the evaluation of the spectra of μ_a and μ_s from the natural muscle is highly important for the present study. By knowing these spectra in a broad range that contains the emission wavelengths of the lasers to use in the transmittance measurements, it will allow to perform an accurate interpretation of the measured intensity-modulated transmittance as a function of wavelength. The same is valid also to discuss the increase in transparency of the muscle samples that will be treated with the four OCA solutions. The spectra of the optical properties of a tissue can be calculated from experimental T_c, total transmittance (T_t) and total reflectance (R_t) spectra [21]. In this study, the calculations were based specifically on the T_c spectra acquired using the experimental setup presented in Fig.

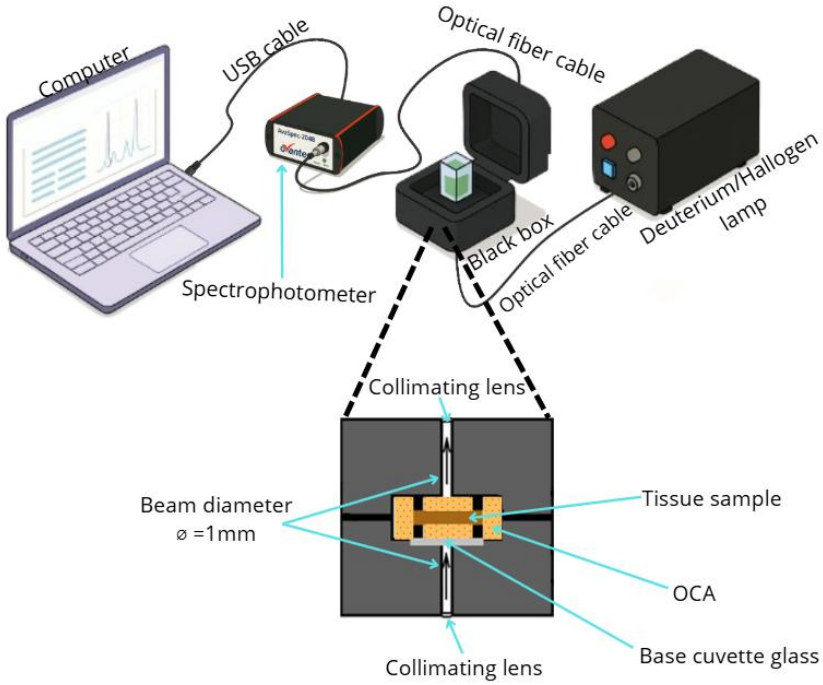

Figure 2 - Experimental setup used to obtain T_c spectra.

The measurements performed with the experimental setup presented in Fig. 2 were conducted as follows. Light emitted from a deuterium-halogen lamp (model AvaLight-D(H)-S, Avantes™, Netherlands) is delivered to the sample cuvette inside the black box through an optical fiber cable and a collimating lens. At the bottom of the sample cuvette there is a pinhole (not seen in Fig. 2) that reduces the diameter of the collimated beam to 1 mm. This beam crosses the glass of the sample cuvette, having this glass a transmittance of 100% between 170 and 2500 nm (UQG Optics, UK). The beam transmitted by the tissue sample is collected by another collimating lens and optical fiber cable to be delivered to the spectrophotometer (model AvaSpec-2048 from Avantes, Apeldoorn, Netherlands), which uses a dedicated software to register the spectrum in a computer.

Before initiating the measurements with the setup presented in Fig. 2 and before placing the tissue sample in the setup, both the noise spectrum (with the lamp turned off) and the reference spectrum (with the lamp turned on) of the setup are recorded for accurate calculation of the T_c and absorbance spectra of the sample. Such calculation is made automatically by the software of the spectrophotometer. Following these initial measurements to calibrate the setup, the measurement of the T_c spectra from muscle samples were initiated. Ten muscle samples were placed inside the sample cuvette, one at a time, and the corresponding spectrum of each sample was measured between 200 and 1000 nm, with 1 nm resolution. These spectra were used to calculate the μ_a and μ_s spectra of the muscle, as explained below in section 3.4.1.

The same setup was used to measure the absorbance spectra of the OCA solutions that will be used to create transparency in the muscle samples. The absorbance spectra obtained in these measurements were firstly used to calculate the μ_a spectra of the OCA solutions by dividing each absorbance spectrum by the sample thickness [35]. Section 3.4.1 describes how the μ_a spectra are used to calculate the anomalous dispersion, both for the muscle and for the OCA solutions.

3.3.2 Laser transmittance measurements and OCAs treatments

One of the objectives of this work was to characterize the attenuation of intensity-modulated laser beams in biological tissues through transmittance measurements, but the main objective was to evaluate the possibility to enhance the tissue transmission of intensity-modulated laser beams by inducing temporary and reversible transparency effects in the tissue, thereby reducing light scattering. Such part of the work is innovative in the context of intensity-modulated laser beams and it was conducted also to compare between the transparency

effects created by 4 OCAs. To achieve the proposed objectives and draw meaningful conclusions, the experimental setup illustrated in Fig. 3 was developed. This configuration enables the measurement of the signal transmitted through the sample, specifically, the portion of the intensity-modulated laser beam that successfully passes through the tissue and reaches the detector.

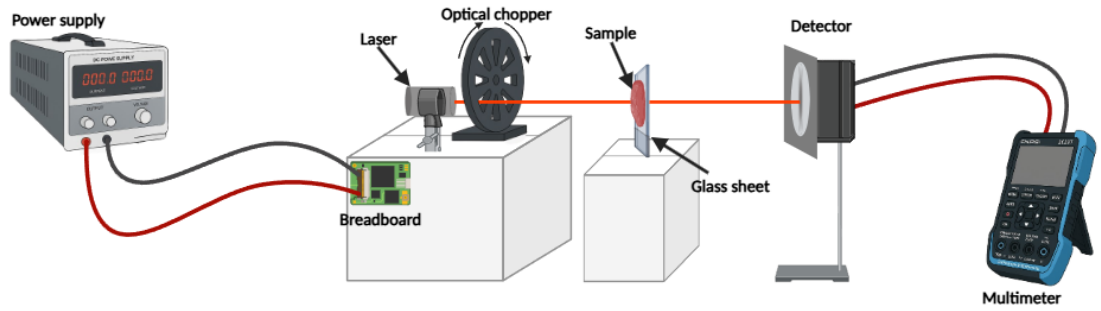

Figure 3 - Experimental setup used to obtain the amount of laser signal that passes through the sample.

To perform the transmittance measurements of the intensity-modulated light from the various lasers, the following material was required to implement the experimental setup represented in Fig. 3: a power supply, a breadboard, various lasers with emission peaks at different wavelengths, an optical chopper, glass sheets, a detector and a portable oscilloscope. To obtain data in any particular tissue/laser configuration, the continuous laser beam was modulated using an optical chopper, which generated an intensity-modulated laser wave with a square form. These intensity-modulated laser beams propagated through air and crossed the sample, as illustrated in Fig. 3. As the intensity-modulated laser wave crosses the sample, a portion of its intensity is attenuated inside the tissue due to scattering and absorption, while the remaining light is transmitted. The transmitted portion of the wave propagates along the optical path until it reaches the slit of the detector. The detected laser wave is converted into an electrical signal, which appears at the screen of the oscilloscope (model 2C53T, FNIRSI, China) as a square form wave corresponding to the measured intensity in volts. It is important to remember that six different lasers were employed in this study, with emission wavelengths at 405 nm, 532 nm, 635 nm, 780 nm, 830 nm, and 850 nm, as indicated by the manufacturer (www.civillasers.com, China). All these lasers are diode lasers, with 5 mW output.

Before initiating the measurements with the setup presented in Fig. 3, and without placing the tissue sample in this setup, the breadboard wires were connected to the power supply to provide power to the optical chopper, and the output voltage was precisely set to 3.211 V. This voltage was selected because it allowed the optical chopper to operate at an optimal speed, neither too slow nor too fast, with a frequency of 250 Hz, which was maintained consistently throughout the study. After that, the laser was securely mounted in its holder and connected to the power source. With the laser turned on, its position was carefully adjusted to ensure precise alignment, directing the beam accurately to the detector's slit. This alignment was performed by monitoring both the visual position of the beam and the peak-to-peak signal amplitude of the generated intensity waves. Once the beam appeared visually centered and the peak-to-peak voltage was maximized, the beam was considered properly aligned. After completing the setup with the establishment of the connection between the detector and the oscilloscope, data acquisition was ready to begin. The measurement process started with the acquisition of the peak-to-peak noise voltage (Vpp_{noise}), in other words, the signal recorded without any tissue placed between the optical chopper and the detector, and the laser turned off. This baseline measurement is essential, as it will be used in the transmittance calculations. Subsequently, the optical chopper and laser were activated, and a glass sheet was positioned between the optical chopper and the detector to record the laser peak-to-peak reference signal (Vpp_{laser}).

After recording these reference values, an untreated tissue sample was placed on the glass sheet to measure its corresponding peak-to-peak voltage (Vpp). This sample was then replaced by another sample and a total of five distinct samples were used in these measurements, keeping the same laser in use and replacing only the sample in the glass sheet for each individual measurement. After completing the five measurements with the first laser, the laser was replaced, and the entire adjustment and reference measurement procedure was repeated for the new laser. With the new laser configured, five Vpp measurements were conducted using the same five tissue samples. This procedure was repeated for each of the six lasers, maintaining the signal detected by the oscilloscope with a square form with pulse duration of 2 ms and a frequency of 250 Hz.

After acquiring the Vpp voltage for all lasers and tissue samples, it was time to treat the tissue samples with an OCA solution to study how tissue transmittance improves as a result of the created transparency. To begin the treatments, 15–20 mL of the OCA solution was added

to each of the five recipients, one for each tissue sample. Each sample was then placed in its corresponding recipient and treated for 30 minutes, as shown in Fig. 4.

Figure 4 - Samples immersed in an OCA solution to create transparency.

After concluding the transparency treatment, the samples were removed from the recipients, and the previously described procedure to measure the post-treatment Vpp voltage for each laser and corresponding sample was repeated. It is essential to note that the second set of post-treatment measurements remained valid, as all initial conditions, including laser alignment, distances between the sample and both the chopper and detector, lighting conditions, and reference peak-to-peak voltages, were consistently maintained. Such measurement procedure was repeated for other samples that were treated with different OCA solutions. For each of those studies, performed by applying a transparency treatment with each of the OCA solutions, five Vpp measurements were performed on different tissue samples using each of the lasers, resulting in a total of 30 measurements per OCA registered before and after treatment.

3.4 Calculation methodology

Once the experimental measurements were acquired, it was necessary to process the experimental data in order to obtain the results and draw conclusions. Accordingly, this section will present in detail all the calculations required to generate those results.

3.4.1 Optical properties of muscle and OCA solutions

Using 10 T_c spectra measured from natural muscle samples as described in section 3.3.1, the μ_a and μ_s spectra of the muscle could be calculated to characterize this tissue in a broad spectral range. Using MATLAB™, the attenuation coefficient spectrum ($\mu_t(\lambda)$) was calculated

between 200 and 1000 nm from the measured T_c spectra. Such calculation was performed through the Bouguer-Beer-Lambert (BBL) equation [26], which establishes a relation between T_c, μ_t and the sample thickness (d). Rearranging this equation as in Eq. (4), it becomes possible to calculate $\mu_t(\lambda)$ from the measured T_c spectrum ($T_c(\lambda)$), as described in other studies [87], [88]:

$$T_c(\lambda) = \exp(-\mu_t(\lambda) \times d) \;\leftrightarrow\; \ln(T_c(\lambda)) = -\mu_t(\lambda) \times d \;\leftrightarrow \mu_t(\lambda) = -\frac{\ln(T_c(\lambda))}{d}, \quad (4)$$

where $T_c(\lambda)$ should be normalized into a scale between 0 and 1 and d was calibrated to be 500 µm for the natural muscle samples.

After calculating $\mu_t(\lambda)$ for each sample with Eq. (4), the $\mu_a(\lambda)$ and $\mu_s(\lambda)$ can be obtained using a simple calculation procedure. The obtained $\mu_t(\lambda)$ presents a baseline that decreases exponentially with increasing wavelength. Such baseline corresponds to $\mu_s(\lambda)$, and for biological tissues it can be described as a combination of the Rayleigh and Mie scattering regimes, as follows [88]:

$$\mu_s(\lambda) = a' \times \left(f_{Ray} \times \left(\frac{\lambda}{500\ nm} \right)^{-4} + (1 - f_{Ray}) \times \left(\frac{\lambda}{500\ nm} \right)^{-b_{Mie}} \right), \quad (5)$$

with a' representing the μ_s of the tissue at 500 nm, f_{Ray} the fractional contribution of Rayleigh scattering, and b_{Mie} is the exponent factor that is associated with the average size of the Mie scatterers. Considering each sample, the CFTOOL of MATLAB™ was used to calculate the corresponding $\mu_s(\lambda)$ according to Eq. (5), which was then subtracted from the calculated $\mu_t(\lambda)$ to obtain the $\mu_a(\lambda)$ of the tissue sample, as follows:

$$\mu_t(\lambda) = \mu_a(\lambda) + \mu_s(\lambda) \quad \leftrightarrow \quad \mu_a(\lambda) = \mu_t(\lambda) - \mu_s(\lambda). \quad (6)$$

To finalize the characterization of the optical properties of the muscle tissue, it was still required to calculate its anomalous dispersion. To proceed with such calculation, the Kramers-Kronig relations that are described in Eqs. (7) and (8) need to be used [89].

$$K_{\text{tissue}}(\lambda) = \frac{\lambda}{4\pi} \times \mu_a(\lambda), \quad (7)$$

$$n_{\text{tissue}}(\lambda_1) = 1 - \frac{2}{\pi}\int_0^{\infty} \frac{\lambda}{\lambda_1} \times \frac{\lambda}{\lambda_1^2 - \lambda^2} K(\lambda_1)\mathrm{d}\lambda_1, \quad (8)$$

with λ representing a fixed wavelength that can be adjusted for a better vertical matching of the anomalous dispersion calculated with Eq. (8) to experimental discrete experimental RI values that are available for the tissue sample. This calculation procedure was performed for 10 muscle samples and the results are presented in Chapter 4.

Considering the OC treatments, when the OCA molecules replace the water molecules in the ISF of the muscle, an increase in the mean RI of the ISF will occur, leading to a RI matching with the other tissue components, and a consequent reduction of the light scattering [90]. According to such phenomena and in the context of the present work, it is required to evaluate both the absorption and the anomalous dispersion of the OCA solutions to justify the observed transmittance variations at the lasers wavelengths after treating the tissue samples. With the exception TZ, all the other OCAs produce transparent and homogeneous aqueous solutions, known to have null absorption ($\mu_a = 0$) in a broad spectral range, from the deep-UV to the NIR [26]. For the case of TZ, an aqueous solution with 55% concentration will have broader absorption spectra from the UV to the visible due to fluorescence [91]. Considering this information, and using the 5 absorbance spectra ($A_b(\lambda)$) measured from each of the OCA solutions, as described in section 3.3.1, the corresponding μ_a spectra were calculated, as follows [22]:

$$\mu_a(\lambda) = \frac{A_b(\lambda)}{d}. \quad (9)$$

For each of the OCA solutions, the mean $\mu_a(\lambda)$ was calculated to characterize its spectral absorption. It should be referred that for the measurements of the A_b spectra of the OCA solutions, 1 mm thickness for each sample was considered (cuvette thickness), meaning that calculations with Eq. (9) were performed using d = 1 mm.

After calculating the mean μ_a spectra for each of the OCA solutions, the corresponding anomalous dispersions were also calculated using Eqs. (7) and (8). These calculations were optimized based on data from literature for the cases of glycerol [92], sucrose [93] and E-cig [92], [94], and based on the RI measurement of the TZ solution that we have performed at 589.6 nm with the Abbe refractometer. Usually, when various discrete RI values are available for one tissue or OCA solution sample, they can be fitted using an appropriate dispersion curve, such as

the Cauchy equation (Eq. (10)), the Conrady equation (Eq. (11)), and the Cornu equation (Eq. (12)) [21]:

$$n_{\text{tissue/OCA}}(\lambda) = A + \frac{B}{\lambda^2} + \frac{C}{\lambda^4}, \tag{10}$$

$$n_{\text{tissue/OCA}}(\lambda) = A + \frac{B}{\lambda} + \frac{C}{\lambda^{3.5}}, \tag{11}$$

$$n_{\text{tissue/OCA}}(\lambda) = A + \frac{B}{(\lambda - C)}, \tag{12}$$

where A, B, and C represent the fitting parameters specific to the Cauchy, the Conrady, or the Cornu equations, respectively.

In the case of the glycerol solution, discrete RI data between 210 and 710 nm, measured at 20°C, were first retrieved from the papers of R. D. Birkhoff *et al.* and V. Gupta *et al.* [92], [95]. Such discrete RI data were fitted with a Cornu-type (Eq. (12)) curve in CFTOOL from MATLAB™, obtaining an R^2 value of 0.9999. This curve is described by Eq. (13).

$$n_{\text{glycerol}}(\lambda) = 1.458 + \frac{5.427}{(\lambda - 180.6)}, \tag{13}$$

Following this estimation of the smooth dispersion for glycerol, its anomalous dispersion curve was directly calculated from the mean $\mu_a(\lambda)$, using Eqs. (7) and (8), to match the curve described in Eq. (13) as much as possible.

For the sucrose solution, the data published by Abebe Gemta and Gido Asefa [93] refers to a solution containing 30% of sucrose, and it is described by the following Cauchy relation:

$$n_{30\%-\text{suc}}(\lambda) = 1.3839 - \frac{0.01611}{\lambda^2} + \frac{0.00516}{\lambda^4}. \tag{14}$$

This way, it was necessary to calculate the corresponding data for the sucrose solution with 64% concentration. To perform such calculation, we first used the Galadstone and Dale equation to obtain the dispersion of pure sucrose ($n_{\text{pure-suc}}(\lambda)$) from the data of the 30%-glucose solution ($n_{30\%\text{-suc}}(\lambda)$) [26]:

$$n_{\text{pure}-\text{suc}}(\lambda) = \frac{n_{30\%-\text{suc}}(\lambda) - 0.7 \times n_{\text{H2O}}(\lambda)}{0.3}, \tag{15}$$

with $n_{H2O}(\lambda)$ representing the dispersion of water for the same spectral range, which was obtained from the paper of Daimon and Matsumura [96], with the following Sellmeier relation:

$$n_{\mathrm{H2O}}(\lambda) = \sqrt{1 + \frac{0.5684\lambda^2}{\lambda^2 - 0.005102} + \frac{0.1726\lambda^2}{\lambda^2 - 0.018212} + \frac{0.0209\lambda^2}{\lambda^2 - 0.026207} + \frac{0.1131\lambda^2}{\lambda^2 - 10.697927}}. \quad (16)$$

After calculating $n_{pure\text{-}suc}(\lambda)$ with Eq. (15), the Gladstone and Dale equation was used once again to calculate the dispersion for the solution containing 64% of sucrose ($(n_{64\%\text{-}suc}(\lambda))$):

$$n_{64\%-\mathrm{suc}}(\lambda) = 0.64 \times n_{\mathrm{pure-suc}}(\lambda) + 0.36 \times n_{\mathrm{H2O}}(\lambda). \quad (17)$$

Using the curve calculated with Eq. (17) as a reference, the anomalous dispersion for the sucrose solution was calculated from its mean $\mu_a(\lambda)$, using Eqs. (7) and (8).

Regarding the E-cig fluid, its dispersion is not available, but it can be easily calculated through the Gladstone and Dale equation, since this commercial product contains 70% of glycerol and 30% of propylene glycol. Retrieving numerical data from the dispersion of propylene glycol at 20°C, between approximately 394 and 1071 nm, from the paper of Daniel Jakubczyk *et al.* [94] , the CFTOOL from MATLAB™ was used to calculate the dispersion curve for this diol (2-alcohols) as:

$$n_{\mathrm{PG}}(\lambda) = 1.418 + \frac{6.841}{(\lambda - 159.4)}. \quad (18)$$

This dispersion curve was obtained with R^2=0.9996, and it can now be used with the dispersion curve of glycerol, described by Eq. (13) to calculate the dispersion of E-cig ($n_{E\text{-}cig}(\lambda)$):

$$n_{\mathrm{E-cig}}(\lambda) = 0.7 \times n_{\mathrm{glycerol}}(\lambda) + 0.3 \times n_{\mathrm{PG}}(\lambda) \quad (19)$$

Considering the dispersion calculated with Eq. (19) for the E-cig fluid, Eqs. (7) and (8) were used once again to obtain its anomalous dispersion from the calculated mean $\mu_a(\lambda)$ of this OCA.

Finally, for TZ solutions, no data regarding its broadband dispersion is already available. Only the RI values of various TZ solutions that we have measured experimentally with the Abbe refractometer, which were published in our recent paper [86], are available. Due to this lack of

such reference data, we considered the measured RI of the TZ solution with 55% concentration at 20°C and at 589.6 nm, which was 1.4326. This single value was used as a reference in the calculations with Eqs. (7) and (8) to obtain the anomalous dispersion for the TZ solution. As a consequence of this procedure, and since the anomalous dispersion of TZ does not present a uniform and smooth wavelength-dependence as the ones observed for the other OCA solutions, no equation to describe the dispersion of the 55%-TZ solution was obtained.

All the absorption spectra and calculated dispersions for the OCA solutions are presented in Chapter 4, and they will allow the interpretation of the transmittance measurements performed with intensity-modulated laser beams.

3.4.2 Transmittance of intensity-modulated laser beams before and after OC treatments

Using the five Vpp voltage values measured from each of the five muscle samples, along with the corresponding Vpp_{laser} and Vpp_{noise} voltage values obtained before and after treatment through the setup described in Section 3.3.2, the data were processed to compare the amount of signal reaching the detector in both conditions, allowing for an evaluation of the effectiveness of each OC treatment. The tissue transmittance (T) of the modulated laser beams was calculated for both cases before and after treatment with the OCAs using the following relation:

$$T = \frac{Vpp - Vpp_{\text{noise}}}{Vpp_{\text{laser}} - Vpp_{\text{noise}}} \times 100\%. \tag{20}$$

Additionally, to gain deeper insight into the performance of the optical clearing agents beyond the comparison of transmittance values before and after treatment, such transmittance values were further used to calculate the optical clearing efficiency ($OC_{eff}(\lambda, t)$) of each treatment as follows [21]:

$$OC_{eff}(\lambda, t) = \frac{|T(\lambda,t) - T(\lambda,t=0)|}{T(\lambda,t=0)} \times 100\% \tag{21}$$

where *t* represents the time of treatment for the samples, which was 30 min in all cases, $T(\lambda, t)$ represents the sample transmittance at a laser wavelength (λ) after the treatment (t = 30 min) and $T(\lambda, t = 0)$ is the sample transmittance at a laser wavelength (λ) before the treatment. All the data that results from these calculations is presented and discussed in Chapter 4.

Chapter 4 - Results and Discussion

4 Results and Discussion

Following the experimental procedures described in the various sections of Chapter 3, the research conducted in this work was performed in a sequential manner. As an example for a one-day study, after preparing the tissue samples in the early morning, the T_c spectra of those samples were acquired with the setup presented in Fig. 2 to calculate the corresponding $\mu_a(\lambda)$ and the $\mu_s(\lambda)$ between 200 and 1000 nm. Since these measurements do not invalidate the samples, they were later used to measure the intensity-modulated transmittance of all lasers with the setup presented in Fig. 3. After completing these measurements with all lasers, the tissue samples were immersed in an OCA solution for 30 min, as represented in Fig. 4 to create transparency. Once these OC treatments were completed, new intensity-modulated transmittance measurements were performed with all lasers. Such procedure was repeated 5 times, using different muscle samples, for each OCA solutions, so that calculations, as described in section 3.4, could be performed to obtain statistical results. Considering the various results obtained in this study, their presentation and discussion will be made also in a sequential manner in the following sections starting with the characterization of the optical properties of the skeletal muscle in section 4.1.

4.1 Spectral optical properties of the muscle

Since various muscle samples were used to measure their T_c spectra for the calculation of the μ_a and μ_s spectra from 200 to 1000 nm, the mean $T_c(\lambda)$ of those samples was calculated and it is presented in Fig. 5.

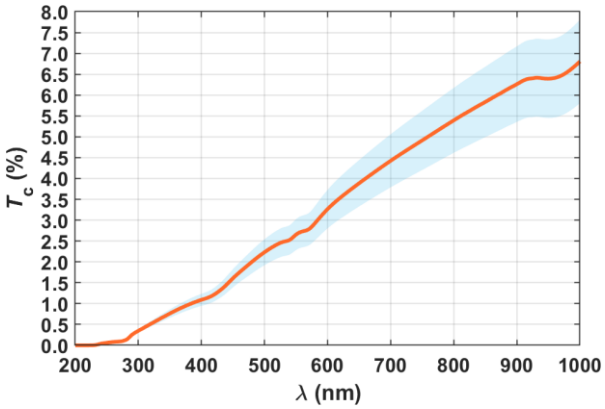

Figure 5 -Mean natural $T_c(\lambda)$, obtained from measurements acquired from 10 samples.

Figure 5 contains a great amount of information regarding the skeletal muscle. Analyzing the mean T_c spectrum, we see that the muscle presents nearly zero-transmittance between 200 and ~280 nm, showing that the combination of strong scattering with the absorption bands of proteins, DNA and hemoglobin in this range are the cause for such strong attenuation [21]. For wavelengths above ~280 nm, T_c increases almost linearly with λ, as already observed for other tissues, including the muscle [21], [29]. The Soret and the Q-bands of hemoglobin are seen in the mean $T_c(\lambda)$ presented in Fig. 5 [31], but they present small magnitude, showing that the blood content in the samples used to acquire these measurements was not too high. The absorption band of water, seen between 900 and 1000 nm presents a significant magnitude, which is real evidence of the 76% volume content of water in the skeletal muscle [97]. Considering the spectral standard deviation (SD) between the measured spectra, that is presented as a blue shade in Fig. 5, it is observed that it also grows with λ. This behavior is consistent with the fact that strong scattering combined with strong absorption bands in the UV in all samples lead to small SD, while different scattering properties between the samples in the NIR lead to a higher magnitude of SD between samples.

Following the calculations described in section 3.4.1, the spectra of μ_a and μ_s were calculated for all samples between 200 and 1000 nm. Eqs. (4), (5) and (6) were used to perform these calculations from the various $T_c(\lambda)$. After calculating all the μ_a/μ_s pairs of spectra for all the 10 samples, the mean and SD for each of these optical properties were calculated and are presented in Fig. 6.

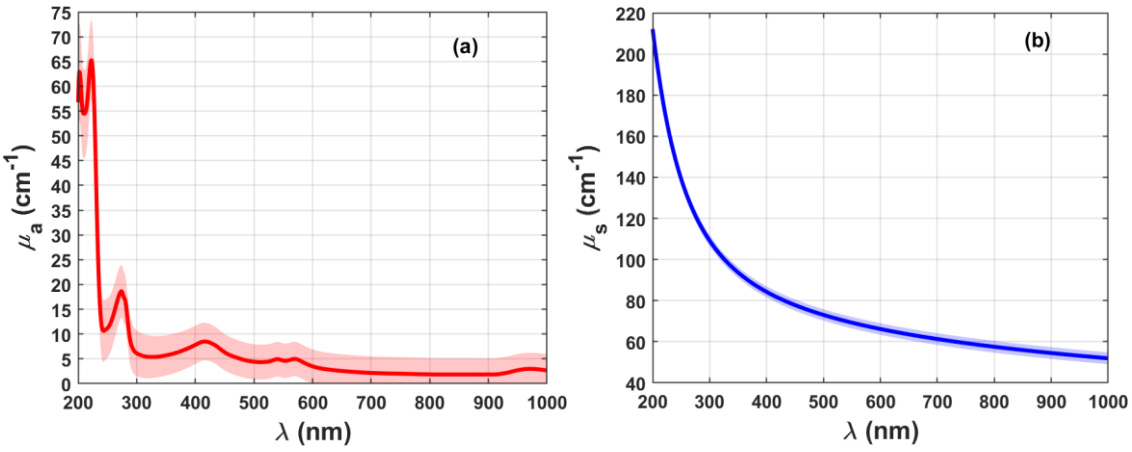

Figure 6 - Mean $\mu_a(\lambda)$ (a) and mean $\mu_s(\lambda)$ (b) for the natural skeletal muscle.

Analyzing the spectral optical properties presented in Fig. 6, it is seen that the mean $\mu_a(\lambda)$ shows real evidence of the absorption bands of proteins, hemoglobin and water. The absorption bands of proteins, with central peaks at 207, 223 and 274/280 nm are clearly seen

in the mean $\mu_a(\lambda)$ presented in Fig. 6(a) [31], [69]. Since the volume content of proteins in the skeletal muscle is 17.7%, and the volume content of DNA/RNA is merely 0.07% [98], the absorption band of DNA/RNA[31], [69], with central peak at 260 nm is hidden by the stronger absorption of proteins. Fig. 6(a) also clearly shows the Soret and the Q-bands of hemoglobin, with central peaks at 415 nm and 540/570 nm [31], indicating that although the samples used in the spectral T_c measurements had low blood content (low magnitude bands in Fig. 6(a)), the hemoglobin is oxygenated. Regarding the absorption band of water seen in Fig. 6(a), it presents low magnitude when compared to the absorption bands of proteins. Considering this fact and also that the water content in the skeletal muscle is 76% [97], we see that the evaluation of absorption band magnitudes from the $\mu_a(\lambda)$ is not a realistic measure of the tissue components concentrations, as previously observed in other studies [33], [99]. This means that if a quantification of the volume contents of tissue components is desired, further calculations are required, as explained by Pinheiro *et al.* [33], [99]. Considering the spectral SD in Fig. 6(a), it is observed that it presents almost constant magnitude between 200 and 1000 nm, indicating that the contents of the various tissue chromophores is similar between the samples used in the spectral T_c measurements.

Regarding the $\mu_s(\lambda)$ of the muscle that is presented in Fig. 6(b), it shows that the mean scattering coefficient presents significantly higher values than the mean absorption coefficient in the entire spectral range. Due to the calculation of the μ_s spectra with Eq. (5), we see from Fig. 6(b) a smooth-exponential decrease in the mean $\mu_s(\lambda)$. Its SD shows the same λ-dependence, but with increasing magnitude from 200 to 1000 nm. Such increase in magnitude indicates that although the scattering is higher in the UV, higher scattering variability between the samples under study is observed in the NIR range, due to the lack of strong absorption bands for longer wavelengths.

As a final comment to the graphs presented in Fig. 6, which will be useful to interpret the results obtained in the transmittance measurements with the various lasers, it is important to refer that for the spectral range that includes the emission wavelengths of those lasers, scattering dominates over absorption. In this spectral range, approximately between 400 and 860 nm, only the absorption bands of hemoglobin are seen in Fig. 6(a). From that figure, the absorption bands of hemoglobin have magnitudes significantly lower than the ones that correspond to proteins. As referred above, such magnitude difference is evidence of the low blood content, when compared to the protein content, in the muscle samples used in this study. This means that the occurrence of the Soret and Q-bands at 415 and 540/570 nm will not be a

significant drawback to the creation of tissue transparency with the different OCA solutions at the laser wavelengths. Hemoglobin is located inside the red blood cells (RBCs), and for OC treatments during only 30 min, the OCA molecules cannot penetrate the membranes of RBCs, leading to a RI matching only outside these cells. An exception to this influence of the absorption bands of hemoglobin in the created transparency might occur for the laser with emission at 405 nm, since this wavelength is very close to the Soret band. When presenting the results for the transmittance of intensity-modulated light from this laser, an analysis of such influence will be performed.

Following the calculation procedure described in section 3.4.1, the μ_a spectra obtained from the skeletal muscle samples were used to calculate the anomalous dispersion of the muscle. The K-K relations, described by Eqs. (7) and (8), were used to perform these calculations, resulting in the mean dispersion for the natural skeletal muscle that is presented in Fig. 7.

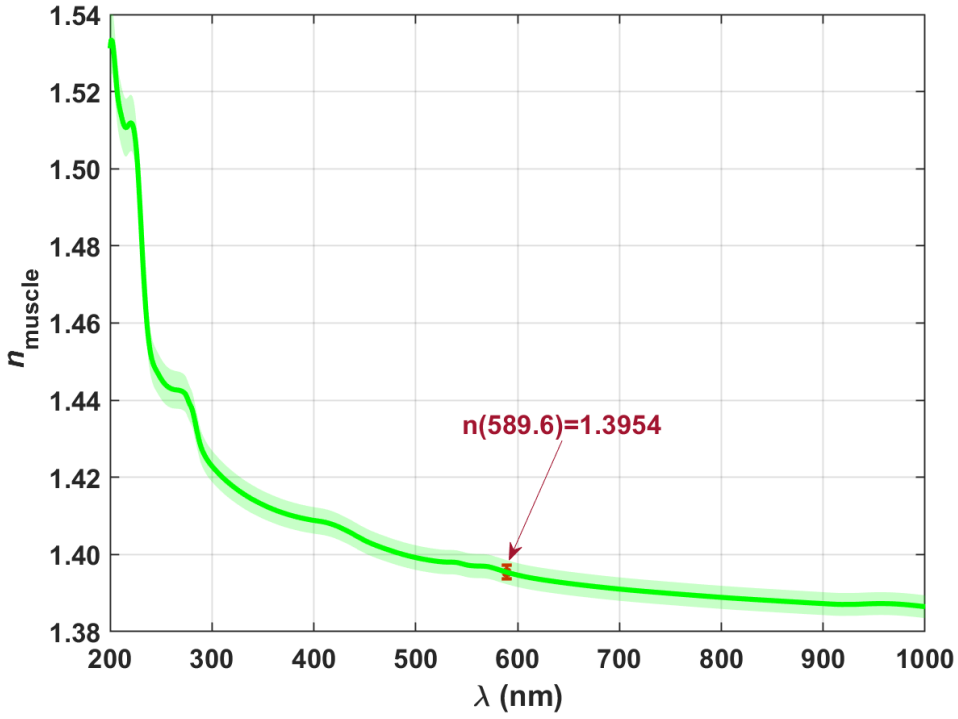

Figure 7 - Anomalous dispersion of skeletal muscle

The red dot with an error bar that is presented in Fig. (7) is the result of RI measurements, performed with an Abbe refractometer (model ORT-1, Kern, Germany), from 5 muscle samples that were being used for another study at the INESC-TEC laboratory. These measurements were performed from muscle samples with 0.4 mm thickness, under red light illumination (λ=633 nm) for better contrast reading, at 20°C and are referred to 589.6 nm [100]. Since the tissue samples used to perform these measurements are also from the skeletal muscle of the rabbit, the

supervisors of this work have suggested that such data should also be used here. The data obtained in those measurements is presented in Table 1:

Table 1 - RI of the skeletal muscle obtained at 589.6 nm.

Skeletal muscle	RI	Mean RI ± SD
Sample 1	1.3950	1.3954±0.0018
Sample 2	1.3925	
Sample 3	1.3960	
Sample 4	1.3965	
Sample 5	1.3970	

From Fig. 7 it is seen that the calculated mean dispersion coincides with the mean RI at 589.6 nm. It is also observed from Fig. 7 that the muscle dispersion shows exponential-decreasing behavior with increasing wavelength, as it has been observed for various other tissues as a result of the dispersions of water and other tissue components [21]. Although having small magnitude, the anomalous dispersion of the muscle presented in Fig. 7 shows evidence of the absorption bands of proteins, hemoglobin and water, as it was seen in the mean μ_a spectrum presented in Fig. 6(a). Once again, from Fig. 7, the absorption bands of hemoglobin have low magnitude in the muscle dispersion, suggesting that they will not condition the transparency created by the various OCAs at the laser wavelengths.

4.2 Spectral characterization of the OCA solutions

For a later interpretation of the transparency created in the muscle samples by the different OCA solutions, it is required to perform an analogous characterization of the absorption and dispersion of the various OCA solutions that will be used. This way, the setup presented in Fig. 2 was used to measure the absorbance spectra of the various OCA solutions that were used in this work. The general procedure used to obtain such characterizing spectra for the OCA solutions is described next.

Considering each OCA solution, 5 absorbance spectra were measured from samples with 1 mm thickness. Such spectra were submitted to calculations with Eq. (9) to obtain the corresponding μ_a spectra. The mean $\mu_a(\lambda)$ was calculated for each OCA solution, as well as the corresponding anomalous dispersion, through the K-K relations presented in Eqs. (7) and (8).

For the case of the 64%-sucrose solution, the calculation of the anomalous dispersion was optimized using a Conrady dispersion curve that provided the best fit of the RI data for this solution after calculations with Eqs. (14) to (17) as described in section 3.4.1. Such Conrady dispersion curve is described by Eq. (22).

$$n_{64\%-\mathrm{suc}}(\lambda) = 1.2279 + \frac{121.0247}{\lambda + 98.5745}, \tag{22}$$

The $\mu_a(\lambda)$ and the anomalous dispersion for the 64%-sucrose solution are presented in Fig. 8.

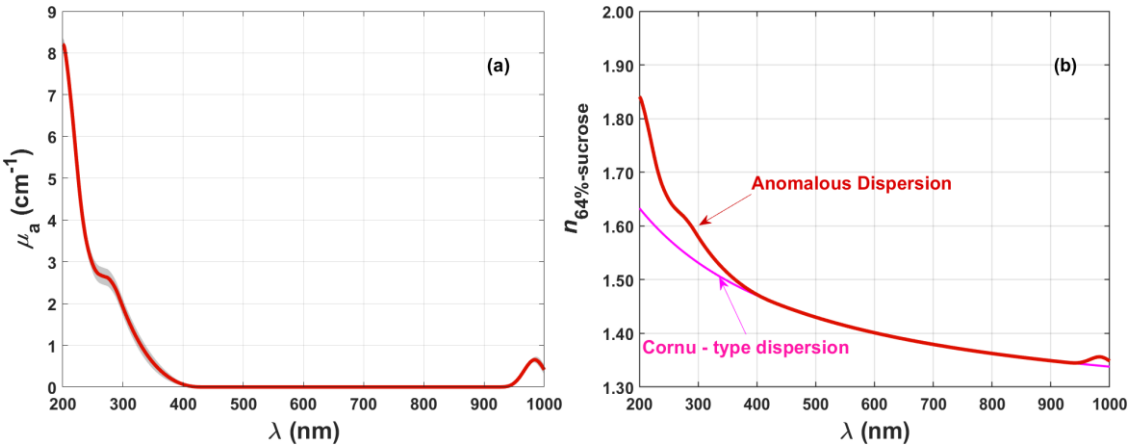

Figure 8 - Mean $\mu_a(\lambda)$ for the 64%-sucrose solution (a), and its anomalous dispersion (b).

According to the $\mu_a(\lambda)$ presented in Fig. 8(a), the 64%-sucrose solution does not present any absorption in the spectral range of interest for the transmittance studies with lasers, which is approximately between 400 and 860 nm. The calculated anomalous dispersion for this solution shows the typical exponential decrease with increasing λ that has been observed in other tissues [21]. It also shows the absorption bands of sucrose and water, but they are located outside the spectral range of interest, meaning that for that spectral range, the RI matching mechanism will occur in an optimized manner for the samples to treat with this solution.

A similar procedure was performed to characterize the 99%-glycerol solution. Its $\mu_a(\lambda)$ was calculated from A_b spectra that were measured from 5 samples with 1 mm thickness, which resulted in the mean $\mu_a(\lambda)$ presented in Fig. 9(a). This mean $\mu_a(\lambda)$ was used to calculate the dispersion of the 99%-glycerol solution through the K-K relations presented in Eqs. (7) and (8). Such calculations with the K-K relations were optimized for this solution using the Cornu-type dispersion described by Eq. (13), which was the best fitting for the discrete RI data of glycerol

retrieved from the papers of R. D. Birkhoff *et al.* and V. Gupta *et al.* [92], [95]. Fig. 9(b) presents such anomalous dispersion.

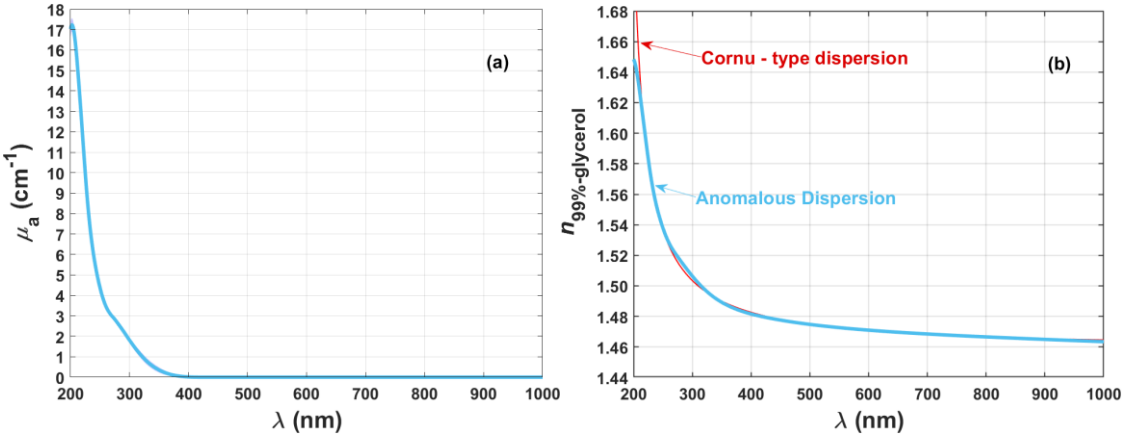

Figure 9 - Mean $\mu_a(\lambda)$ for the 99%-glycerol solution (a), and its anomalous dispersion (b).

Both graphs in Fig. 9 show similar shape to the ones presented in Fig. 8 for the 64%-sucrose solution. The mean $\mu_a(\lambda)$ presented in Fig. 9(a) only shows the absorption band of glycerol, which is located between 200 and ~380 nm. No absorption band for water is seen in this graph, which is perfectly expected, since in this solution there is only 1% of water that was captured by glycerol molecules from the humidity in the air. Once again, this solution of glycerol presents no absorption in the spectral range of interest for the measurements of intensity-modulated transmittance with the lasers, and its spectral SD is too small to see, which shows that the various samples had very similar A_b spectra. The anomalous dispersion that is presented in Fig. 9(b) presents the same quality as described for the anomalous dispersion of the 64%-sucrose solution, since both present a similar shape without any absorption bands in the spectral range of interest. Furthermore, for the case of the 99%-glycerol solution, its anomalous dispersion presents higher values than the ones observed for the 64%-sucrose solution, meaning that for the study where glycerol is used as an OCA, a better RI matching than the one induced by the sucrose solution is to be expected.

Moving to the E-cig fluid, a similar procedure was performed to obtain its mean $\mu_a(\lambda)$ and its anomalous dispersion. Following the experimental procedure described in section 3.4.1, the A_b spectra of five samples of the E-cig fluid with 1 mm thickness were measured to calculate the $\mu_a(\lambda)$ for this solution with Eq. (9). The calculated mean $\mu_a(\lambda)$ is presented in Fig. 10(a). After obtaining the mean $\mu_a(\lambda)$ for the E-cig solution, it was used to calculate the corresponding anomalous dispersion with Eqs. (7) and (8). Once again, the optimization of these calculations was made through the use of the estimated dispersion for E-cig, as calculated with Eq. (19) from

the dispersions of glycerol and propylene glycol in the 70%/30% proportions. The anomalous dispersion of the E-cig fluid is presented in Fig. 10(b).

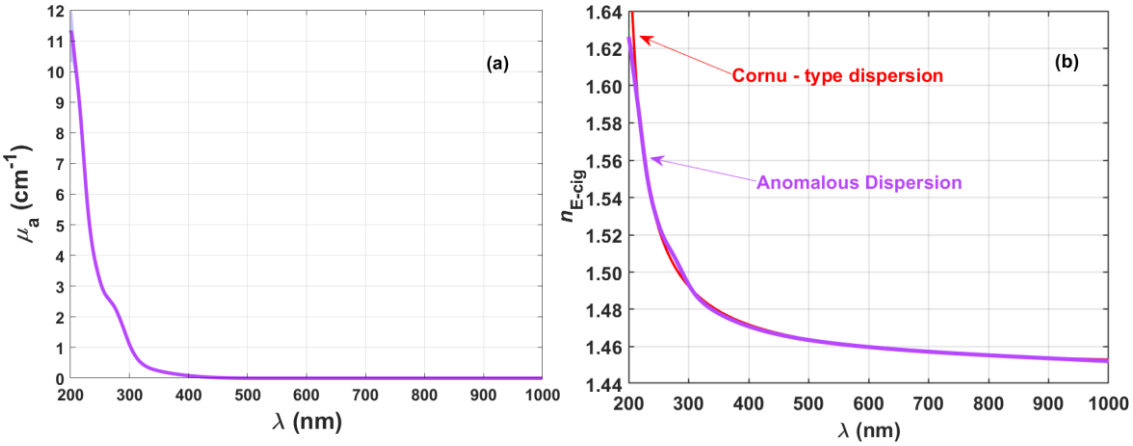

Figure 10 - Mean $\mu_a(\lambda)$ for the E-cig solution (a), and its anomalous dispersion (b).

Once again, when analyzing the graphs presented in Fig. 10, due to the fact that so far we have studied transparent OCAs, the shape of both graphs is similar to the ones presented for the 64%-sucrose and 99%-glycerol solutions. Regarding the $\mu_a(\lambda)$ of the E-cig fluid, the combined absorption band of glycerol and propylene glycol is a little broader than the one observed for the 99%-glycerol solution, but considering the spectral range of interest for the transmittance measurements with the lasers, there is no significant absorption that might influence the creation of tissue transparency in the muscle samples. Once more, due to the 70%/30% combination of glycerol and propylene glycol, there is no absorption band for water in the $\mu_a(\lambda)$ presented in Fig. 10(a). Considering the anomalous dispersion presented in Fig. 10(b), we see similar λ-dependence to the one obtained for the 99%-glycerol solution, but now with smaller values. The addition of 30% of propylene glycol to create the E-cig fluid is the reason to see lower values than the ones previously presented for the 99%-glycerol solution.

The final solution used to create transparency in the muscle samples was an aqueous solution containing 55% of TZ. As previously mentioned in the Introduction, TZ is an absorbing food dye, that has been reported to have absorption bands located in the UV-visible range [91]. Considering such reference to the location of the absorption bands of TZ in this range, it is crucial to measure its absorbance spectrum and identify where these bands are located with precision. Their location may affect the creation of transparency with the lasers used in this work. Considering these facts, 5 A_b spectra were measured from a solution containing only 1.81% of TZ, and another 5 were measured from the solution containing 55% of TZ for comparison. Considering that these spectra were measured from samples with thickness of 1

mm, the corresponding $\mu_a(\lambda)$ for each sample was calculated through Eq. (9). The mean $\mu_a(\lambda)$ for both TZ solutions are presented in Fig. 11(a) for comparison. Following the same procedure that was adopted for the other OCAs, the anomalous dispersion for the 55%-TZ solution was calculated from its mean $\mu_a(\lambda)$, using the K-K relations presented in Eqs. (7) and (8). The reference value used to optimize such calculation was the RI measured from the 55%-TZ solution with the Abbe refractometer, which is 1.4326 at 589.6 nm. The result of these calculations, as well as the RI measured at 589.6 nm are presented in Fig. 11(b).

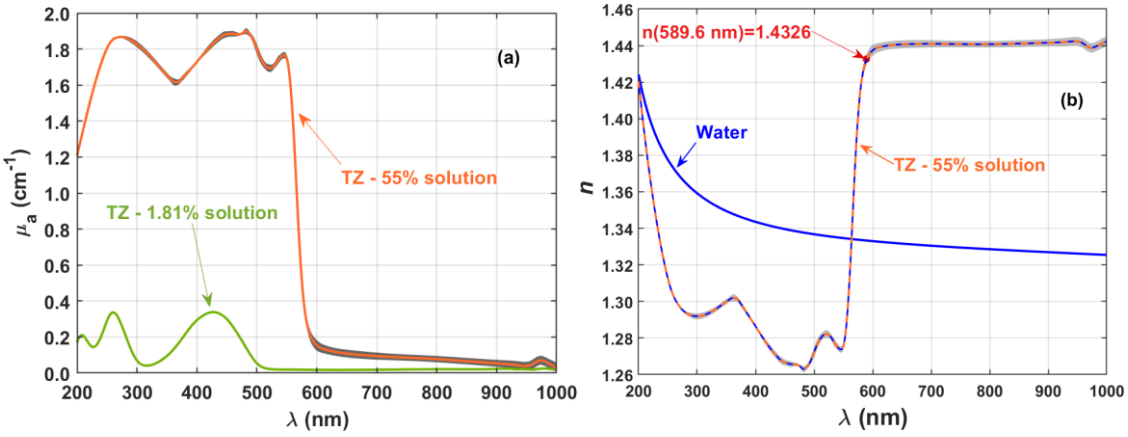

Figure 11 - Mean μ_a spectra for the 1.81%- and 55%-TZ solutions (a), and the anomalous dispersion for the 55%-TZ solution (b).

Comparing between the μ_a spectra presented in Fig. 12(a), it is seen that the low concentrated TZ solution presents 3 absorption bands with central peaks at 208, 260 and 427 nm, while the TZ solution with 55% does not present such structure. Instead, for this highly-concentrated solution, in addition to the absorption band of water, TZ presents a broad absorption band with local maxima at 273 nm, 482 nm, and 545 nm. Such change in the absorption spectra of TZ solutions is due to the occurrence of fluorescence, as previously reported [91], which increases with the TZ concentration in the solution. By having such high absorption between 200 and 600 nm, the 55%-TZ solution is not expected to create significant transparency for this spectral range. This means that when studying the OC effect with lasers emitting within this range, tissue darkening might occur. Considering the anomalous dispersion presented in Fig. 12(b), significant differences are observed when comparing with the anomalous dispersions previously presented for the other OCAs. By presenting the water dispersion in the same graph to be considered as a reference, due to the strong absorption that the 55%-TZ solution presents at low wavelengths, its anomalous dispersion is located below the water dispersion between 200 and 564 nm. According to Fig. 12(b), the anomalous dispersion

of TZ increases fast from 547 to 600 nm, stabilizing for longer wavelengths. The fast increase seen for the anomalous dispersion of this TZ solution in the visible range is the result of the Lorentz-oscillator model for dielectric particles, as previously reported [79]. Such behavior indicates that for the spectral range between 547 and 600 nm, the RI matching mechanism will increase fast, and that for λ > 600 nm high magnitude transparency is expected to occur in tissues treated by this solution.

4.3 Transmittance of intensity-modulated laser beams

After characterizing the skeletal muscle and the OCA solutions in terms of their optical properties, the results obtained in the study of laser transmittance with intensity-modulated beams will be presented. All lasers used in this work had 5 mW output power, and the first step in this study was to confirm the emission wavelengths of those lasers. According to the manufacturer (Civil Lasers, www.civillasers.com, China), these lasers present their emission at certain wavelengths, but measuring their emission with a spectrophotometer, it was verified that the information provided by the manufacturer is not accurate. Table 2 presents the emission wavelengths of the six lasers, as indicated by the manufacturer ($\lambda_{manufacturer}$) and as measured ($\lambda_{measured}$) at the INESC-TEC lab.

Table 2 - Emission peak of the various lasers used in this research.

	$\lambda_{manufacturer}$ (nm)	$\lambda_{measured}$ (nm)
Laser 1	405	405.2
Laser 2	532	520.4
Laser 3	635	640.6
Laser 4	780	782.0
Laser 5	830	819.8
Laser 6	850	851.3

By evaluating the real emission wavelengths for the six lasers will allow to provide accurate results for the intensity-modulated transmittance measurements that will be presented next. Using the experimental setup presented in Fig. 3, the optical chopper was set to a rotation speed, so that the laser pulses that reach the tissue sample had a frequency of 250 Hz and a duty cycle of ~50%. Since this frequency was adopted for all measurements, Fig. 12 shows a characterization of the signals measured by the oscilloscope in DC mode, comparing the

continuous and intensity-modulated modes. These results provide insight into whether the laser beam delivery mode influences the measurements.

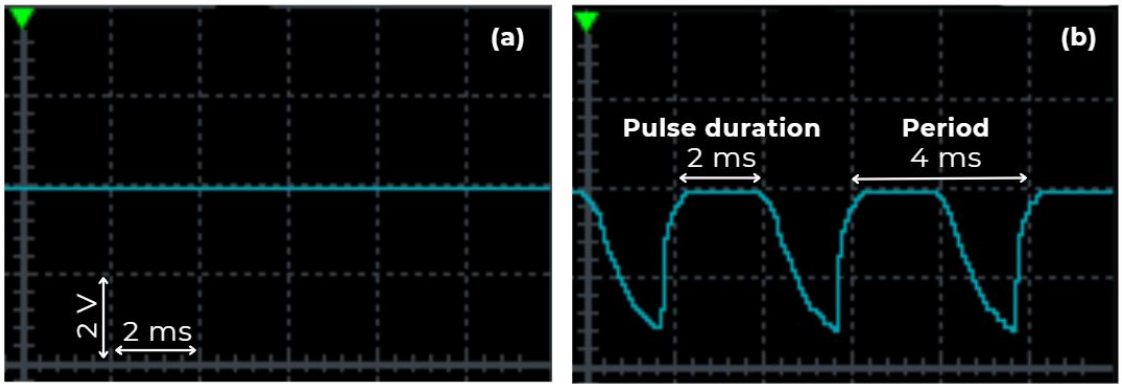

Figure 12 – Comparison between the results obtained for the 632 nm lasers in continuous (a) and intensity-modulated (b) modes.

Analyzing the signals presented in Fig. 12, it is observed that in (a) the intensity is constant in time and has an approximate value of 4 V. In Fig. 12 (b), the signal presents an almost square form with 2 ms duration and 4 ms period, corresponding to a duty cycle of approximately 50%. However, this square-shaped signal is not perfect, having rounded edges and smooth transitions. This is because the detector doesn't respond instantly to the intensity variation, and as the laser passes through the chopper, part of the light is gradually blocked, generating gradual transitions rather than instantaneous ones. Comparing both signals, it is observed that both have very similar magnitudes, showing that by changing from continuous emission to intensity-modulated does not change the amplitude of the detected signal.

An additional comparative analysis was performed using the same setup to evaluate whether the two operation modes produce different interactions with the tissue, potentially leading to variations in transmittance values. Figure 13 shows the transmittance values calculated using Eq. (20) and with the tissue placed between the detector and the laser beam for both operation modes: continuous and intensity-modulated.

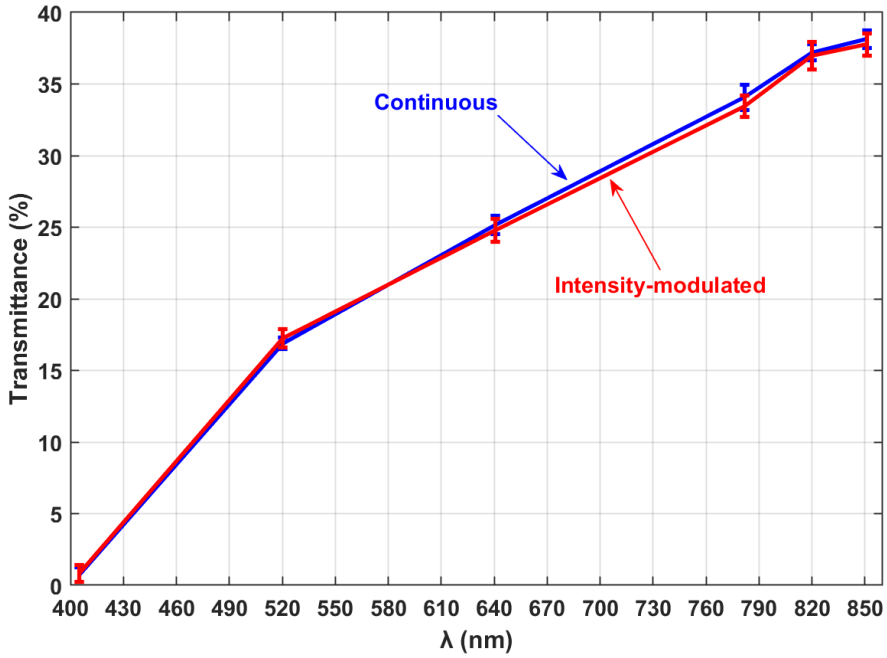

Figure 13 - Transmittance values measured with the tissue placed between the optical chopper and the detector for both operation modes: continuous and intensity-modulated.

Figure 13 shows that there are no significant differences between the two modes in terms of transmittance results. This means that the difference in transmittance measurements collected from the treated tissues that will be presented in the following section are due only to the impact of the different OCAs in the tissue samples. On the other hand, if we compare the data in Fig. 13 with the mean T_c spectrum of the natural muscle that was presented in Fig. 5, we see that the setup used to measure the transmittance with the intensity-modulated laser beams produces similar spectral shape, but high values for the muscle transmittance. This means that the transmittance measurements performed with the setup presented in Fig. 3 do not correspond to T_c. We tried to identify the sources of such high transmittance values that were obtained with the setup presented in Fig. 3, and concluded that it can be optimized for future T_c measurements with the intensity-modulated laser beams, by making some adjustments. In this verification, we found that at the exit of the various lasers, the laser beam is not completely collimated, nor narrow, as in the case of the T_c measurements made with the setup presented in Fig. 2, where the diameter of the light beam is collimated and with a diameter of 1 mm. The aperture of detector used for the measurements with the lasers is 1 cm, but it contains a vertical slit at its entrance that can be adjusted to reduce the thickness of the beam that is collected to 1 mm. Due to the divergence in the laser beam that crosses the optical chopper, when the beam crosses the muscle sample, such divergence will be expanded due to light scattering inside the

sample. This way, when the beam reaches the detector, due to the vertical slit at the entrance, a planar beam with 1 mm thickness and some millimeters in length is collected, leading to the high values of muscle transmittance that were obtained in this study. Although this lack of optimization in the setup presented in Fig. 3 was identified, it does not go against the objectives of this research, since we have verified from Fig. 13 that no significant changes are observed between the measurements performed in the continuous mode and in the intensity-modulated mode, and also due to the fact that the measuring conditions were kept unchanged from the measurements performed from the natural samples to the ones performed from the treated samples. By keeping the same measurement conditions, both in the measurements performed from untreated and treated samples, although all transmittance values do not correspond to T_c, they will prove the creation of transparency at the various laser wavelengths as a result of treating the samples with the various OCAs. For future measurements with the setup presented in Fig. 3, if T_c measurements are intended, a pinhole with Φ = 1 mm should be placed just in front of the tissue sample, on the laser side, and a similar pinhole should be placed in front of the detector to guarantee that a collimated beam is detected. To improve even better such setup to perform T_c measurements, it is recommended to replace the glass that supports the tissue sample by a plastic material with a hole at the center to allow the transmitted laser beam to continue its path to the detector without any reflections.

4.3.1 Study of muscle transmittance before and after treatment with the 64%-sucrose solution

The first study to evaluate the muscle transmittance of intensity-modulated laser beams before and after OC treatment was performed using the 64%-sucrose solution. As previously described, these studies to obtain laser transmittance were conducted using 5 muscle samples per laser, and measurements were performed before and after applying the OC treatment to the tissue samples. Table 3 presents the data acquired from the muscle samples that were treated with the 64%-sucrose solution, specifically the peak-to-peak voltage measured with the setup, but without the tissue sample ($V_{pplaser}$), the peak-to-peak voltage that corresponds to noise, in the laser-off position ($V_{pp\text{-}noise}$), and the peak-to-peak voltage measured after crossing the tissue sample (V_{pp}), both before and after treating the samples.

Table 3 - Peak-to-peak voltage measurements before and after the OC treatment with the 64%-sucrose solution.

λ (nm)	sample	$V_{pplaser}$ (V)	$V_{pp\text{-}noise}$ (V)	V_{pp} (V)		$V_{pplaser}$ (V)	$V_{pp\text{-}noise}$ (V)	V_{pp} (V)
	1			0.06				0.11
	2			0.06	⇒			0.11
405.2	3	1.30	0.05	0.06	⇒	1.32	0.05	0.13
	4			0.06	⇒			0.13
	5			0.06				0.11
	1			0.45				0.94
	2			0.43	⇒			0.92
520.4	3	2.45	0.05	0.47	⇒	2.45	0.05	0.96
	4			0.48	⇒			0.96
	5			0.43				0.90
	1			0.66				1.21
	2			0.64	⇒			1.19
640.6	3	2.45	0.05	0.62	⇒	2.45	0.05	1.15
	4			0.66	⇒			1.13
	5			0.68				1.15
	1			1.00				1.58
	2			0.98	⇒			1.58
782.0	3	2.87	0.05	1.00	⇒	2.87	0.05	1.56
	4			1.02	⇒			1.60
	5			0.96				1.62
	1			1.13				1.70
	2			1.11	⇒			1.72
819.8	3	3.05	0.05	1.13	⇒	3.04	0.05	1.75
	4			1.17	⇒			1.73
	5			1.15				1.73
	1			1.02				1.53
	2			1.04	⇒			1.55
851.3	3	2.62	0.05	0.98	⇒	2.62	0.05	1.53
	4			1.00	⇒			1.47
	5			0.96				1.45

The arrows in the middle column of Table 3 indicate the treatment of the samples, by immersing them in the 64%-sucrose solution. The data in the columns to the left of this middle column represent the measurements performed from the samples before applying the OC treatment, while the columns to the right represent the measurements performed from the samples after 30 min immersion in the OCA solution.

Considering the experimental data in Table 3, calculations were performed with Eq. (20) to obtain the transmittance (T) of the muscle samples when crossed by intensity-modulated laser beams. Using these transmittance values, Eq. (21) was used to calculate the OC_{eff}. All these values are presented in Table 4.

Table 4 - Muscle transmittance of intensity-modulated laser before and after treatment with the 64%-sucrose solution and OC_{eff}.

λ (nm)	sample	T (%)	$\bar{T} \pm$ SD		T (%)	$\bar{T} \pm$ SD	$\overline{OC}_{eff} \pm$ SD
	1	0.800			4.724		
	2	0.800		⇒	4.724		
405.2	3	0.800	0.800 ± 0.00	⇒	6.299	5.354 ± 0.77	569.3 ± 96.4
	4	0.800		⇒	6.299		
	5	0.800			4.724		
	1	16.67			37.08		
	2	15.83		⇒	36.35		
520.4	3	17.50	16.75 ± 0.85	⇒	37.92	36.92 ± 0.97	120.7 ± 5.98
	4	17.92		⇒	37.92		
	5	15.83			35.42		
	1	25.42			48.33		
	2	24.58		⇒	47.50		
640.6	3	23.75	25.08 ± 0.85	⇒	45.83	46.50 ± 1.22	85.60 ± 8.09
	4	25.42		⇒	45.00		
	5	26.25			45.83		
	1	33.69			54.26		
	2	32.98		⇒	54.26		
782.0	3	33.67	33.40 ± 0.72	⇒	53.55	54.54 ± 0.72	63.37 ± 4.96
	4	34.40		⇒	54.96		
	5	32.27			55.67		
	1	36.00			55.19		
	2	35.33		⇒	55.85		
819.8	3	36.00	36.27 ± 0.68	⇒	56.86	56.05 ± 0.54	54.61 ± 2.95
	4	37.33		⇒	56.19		
	5	36.67			56.19		
	1	37.74			57.59		
	2	38.52		⇒	58.37		
851.3	3	36.19	36.97 ± 1.10	⇒	57.59	56.65 ± 1.51	53.31 ± 3.25
	4	36.96		⇒	55.25		
	5	35.41			54.47		

After obtaining the data in Table 4, it was possible to generate the graphs presented in Fig. 13, which present the transmittance of the intensity-modulated laser beams as a function of wavelength (Fig. 13(a)), and the OC_{eff} as a function of wavelength (Fig. 13(b)) for the treatment with 64%-sucrose solution.

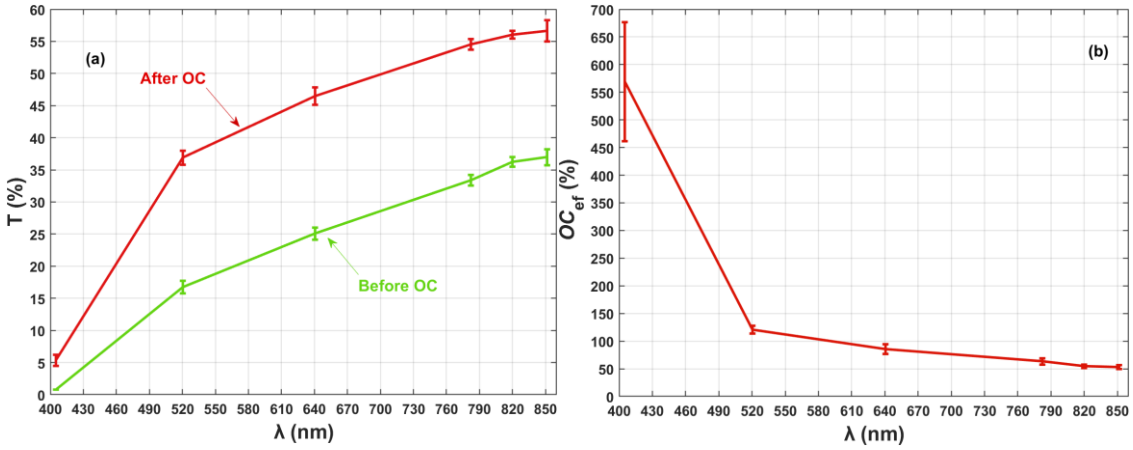

Figure 14 -Muscle transmittance as a function of laser wavelength before and after treatment with the 64%-sucrose solution (a), and OC_{eff} as a function of laser wavelength.

Analyzing Figure 14 (a), we see that the muscle transmittance increases with wavelength, both for the untreated and treated tissue samples. Such wavelength dependence of the muscle transmittance in the untreated sample is imposed by the optical properties of the muscle (μ_a, μ_s and dispersion), which are stronger at lower wavelengths [26]. After the treatment with the 64%-sucrose solution, the RI matching mechanism leads to an increase of muscle transmittance in the whole spectral range, as seen in Fig. 14(a), but since in the untreated tissue, μ_s decreases exponentially with the increase of wavelength, the efficiency of the RI matching mechanism to reduce light scattering is higher at short wavelengths [35]. Such higher efficiency is seen in Fig. 14(b), where OC_{eff} decreases with increasing wavelength. Fig. 14(a) also shows that the muscle transmittance at 405 nm deviates from the trend observed with the other lasers wavelengths. This discrepancy is attributed to the presence of the Soret band, a strong absorption characteristic of hemoglobin, which leads to increased absorption at 405 nm and consequently lower transmittance for this laser. For higher wavelengths, up to 850 nm, the muscle does not present significant absorption bands, with the exception of the Q-bands of hemoglobin. In the case of the muscle samples used in the measurements, the blood content is not high, meaning that the Q-bands are almost not seen, turning the scattering the predominant mechanism of light attenuation for longer wavelengths [21]. As a result, the muscle transmittance is almost linear for the untreated tissue between 520 and 850 nm, as seen in Fig. 14(a). On the other hand, since the dispersion of the 64%-sucrose solution does not present absorption bands in this spectral range (see Fig. 8), after the treatment is applied, the almost linear increase of muscle transmittance with the wavelength is maintained, as a result of the unique scattering reduction for longer wavelengths.

Looking at Fig. 14(b) in more detail, we see that the OC_{eff} presents a decreasing wavelength dependence. In fact, if we had performed measurements with additional lasers with emission wavelengths between 405 and 520 nm, we should see that the OC_{eff} would present an almost exponential decrease with the increasing wavelength. It is worth to remind that both the μ_s of tissues and the dispersions of their components (the ISF and scatterers) have an exponential decreasing behavior with increasing wavelength [21]. During the treatment, as the sucrose molecules replace the water molecules in the ISF, the RI matching mechanism takes place to reduce light scattering, but since the dispersion of sucrose is higher than the dispersion of water in all the spectral range considered in this study (see Figs. 8 and 11), the efficiency of the RI matching mechanism will also be higher for short wavelengths. The wavelength dependence observed in Fig. 14(b) for OC_{eff} translates well the occurrence of the RI matching mechanism and how such matching depends on the wavelength. It can also be said that since the OC_{eff} does not depend on the shape of the transmittance measured from the muscle sample, it translates with high accuracy the impact of the OCA in the tissue.

Similar results were obtained for the treatments with the other OCA solutions, with the exception of the study with TZ, due to the fact that such food dye presents different absorption and dispersion characteristics when compared to the common OCAs. The results obtained with such OCA solutions are presented in the following sub-sections.

4.3.2 Study of muscle transmittance before and after treatment with the 99%-glycerol solution

The second study to evaluate the muscle transmittance of intensity-modulated laser beams before and after OC treatment was conducted using a 99%-glycerol solution. The procedure for data acquisition followed the same methodology described in the first study, and the corresponding results are presented in Table 5.

Table 5 - Peak-to-peak voltage measurements before and after the OC treatment with the 99%-glycerol solution.

λ (nm)	sample	$V_{pplaser}$ (V)	$V_{pp\text{-}noise}$ (V)	V_{pp} (V)		$V_{pplaser}$ (V)	$V_{pp\text{-}noise}$ (V)	V_{pp} (V)
	1			0.06				0.14
	2			0.06	⇒			0.12
405.2	3	1.27	0.05	0.06	⇒	1.25	0.05	0.12
	4			0.06	⇒			0.12
	5			0.06				0.11
	1			0.47	⇒			1.07
	2	2.44	0.05	0.48	⇒	2.45	0.05	1.06
520.4	3			0.48	⇒			1.03

	4			0.48			1.05
	5			0.47			1.00
	1			0.64			1.24
	2			0.65	⇒		1.19
640.6	3	2.41	0.05	0.63	⇒	2.42	0.05	1.17
	4			0.63	⇒		1.20
	5			0.62			1.19
	1			0.99			1.66
	2			1.02	⇒		1.68
782.0	3	2.86	0.05	0.99	⇒	2.85	0.05	1.57
	4			0.96	⇒		1.67
	5			1.01			1.64
	1			1.14			1.88
	2			1.18	⇒		1.87
819.8	3	3.02	0.05	1.14	⇒	3.03	0.05	1.74
	4			1.11	⇒		1.82
	5			1.15			1.82
	1			1.04			1.64
	2			1.02	⇒		1.63
851.3	3	2.65	0.05	1.06	⇒	2.65	0.05	1.59
	4			1.01	⇒		1.61
	5			1.04			1.62

As in the first study, the data were processed using Eq. (20) to calculate the transmittance of the muscle samples when crossed by intensity-modulated laser beams. Based on these transmittance values, Eq. (21) was applied to determine the OC_{eff} produced by glycerol in the muscle. The resulting values are presented in Table 6.

Table 6 – Muscle transmittance of intensity-modulated laser before and after treatment with the 99%-glycerol solution and OC_{eff}.

λ (nm)	sample	T (%)	$\bar{T} \pm$ SD		T (%)	$\bar{T} \pm$ SD	$\overline{OC}_{eff} \pm$ SD
	1	0.820			7.500		
	2	0.820		⇒	5.833		
405.2	3	0.820	0.820 ± 0.00	⇒	5.833	6.000 ± 0.82	632.0 ± 99.6
	4	0.820		⇒	5.833		
	5	0.820			5.000		
	1	17.57			42.50		
	2	17.99		⇒	42.08		
520.4	3	17.99	17.82 ± 0.21	⇒	40.83	41.33 ± 1.03	131.9 ± 5.86
	4	17.99		⇒	41.66		
	5	17.57			39.58		
	1	25.00			50.21		
	2	25.42		⇒	48.10		
640.6	3	24.58	24.75 ± 0.43	⇒	47.26	48.44 ± 0.98	95.79 ± 4.37
	4	24.58		⇒	48.52		
	5	24.15			48.10		
	1	33.45			57.50		

	2	34.52		⇒	58.21		
782.0	3	33.45	33.59 ± 0.73	⇒	54.29	56.93 ± 1.40	69.54 ± 5.54
	4	32.38		⇒	57.86		
	5	34.16			56.79		
	1	36.70			61.41		
	2	38.05		⇒	61.07		
819.8	3	36.70	36.84 ± 0.76	⇒	56.71	59.60 ± 1.67	61.83 ± 4.66
	4	35.69		⇒	59.40		
	5	37.04			59.40		
	1	38,08			61.15		
	2	37,31		⇒	60.77		
851.3	3	38,85	37.85 ± 0.67	⇒	59,23	60.31 ± 0.66	59.41 ± 3.79
	4	36,92		⇒	60.00		
	5	38,08			60.38		

As in the study with the 64%-sucrose solution, the data in Table 6 was used to generate the graphs presented in Fig. 15, where the muscle transmittance, before and after the treatment are presented in Fig. 15(a) and the OC_{eff} is presented in Fig. 15(b).

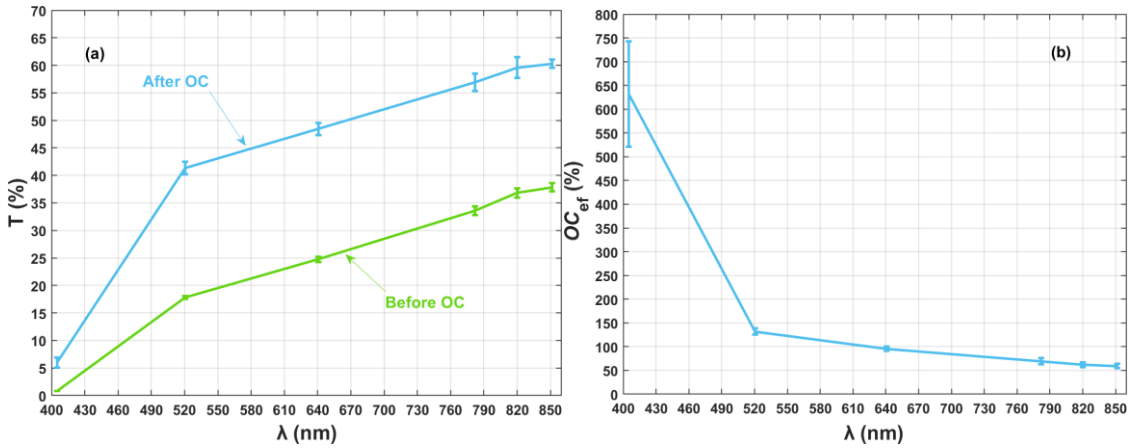

Figure 15 -Muscle transmittance as a function of laser wavelength before and after treatment with the 99%-glycerol solution (a), and OC_{eff} as a function of laser wavelength.

A first analysis of the graphs presented in Fig. 15, shows similar wavelength dependencies for the muscle transmittance and OC_{eff} to the ones obtained for the treatment with 64%-sucrose (see Fig. 14). Considering the data presented in Fig. 15(a), it is observed that the 99%-glycerol solution induced a substantial increase in muscle transmittance. This increase in transparency is consistent with that observed for sucrose, and can therefore be attributed to the same underlying mechanisms that were discussed in the previous sub-section. Comparing between the graphs in Fig. 15 and the ones in Fig. 14, we see that the created transparency at all laser wavelengths is higher in the treatment with 99%-glycerol than in the treatment with 64%-sucrose. Looking at the OC_{eff} presented in Fig. 15(b), we see that indeed glycerol molecules

created a higher impact in reducing light scattering in muscle than sucrose. Such higher efficiency of the RI matching mechanism created by glycerol is observed for all laser wavelengths, but is significantly higher than the one observed for sucrose at 405 nm, where the OC_{eff} was only 550%. Such difference is due to the higher dispersion of the glycerol solution with regard to the dispersion of the sucrose solution (see Figs. 8 and 9), and consequent higher RI matching provided by glycerol at low wavelengths.

4.3.3 Study of muscle transmittance before and after treatment with the E-cig fluid

The third study to evaluate the muscle transmittance with intensity-modulated lasers was conducted with samples that were treated with E-cig fluid. By performing the measurements under the same conditions as in the previous studies, the V_{pp} values were acquired, both for the untreated and the treated muscle samples. Table 7 presents such data.

Table 7 - Peak-to-peak voltage measurements before and after the treatment with the E-cig solution.

λ (nm)	sample	$V_{pplaser}$ (V)	$V_{pp\text{-}noise}$ (V)	V_{pp} (V)		$V_{pplaser}$ (V)	$V_{pp\text{-}noise}$ (V)	V_{pp} (V)
	1			0.06				0.13
	2			0.06	⇒			0.13
405.2	3	1.27	0.05	0.06	⇒	1.27	0.05	0.14
	4			0.06	⇒			0.16
	5			0.06				0.14
	1			0.44				1.10
	2			0.44	⇒			1.07
520.4	3	2.45	0.05	0.44	⇒	2.45	0.05	1.11
	4			0.44	⇒			1.13
	5			0.48				1.10
	1			0.56				1.25
	2			0.59	⇒			1.26
640.6	3	2.42	0.05	0.58	⇒	2.43	0.05	1.25
	4			0.60	⇒			1.24
	5			0.60				1.28
	1			0.89				1.71
	2			0.88	⇒			1.73
782.0	3	2.86	0.05	0.94	⇒	2.85	0.05	1.67
	4			0.92	⇒			1.70
	5			0.94				1.73
	1			1.07				1.93
	2			1.08	⇒			1.92
819.8	3	3.05	0.05	1.10	⇒	3.05	0.05	1.89
	4			1.07	⇒			1.87
	5			1.07				1.90
	1			0.98	⇒			1.65
	2	2.64	0.05	0.97	⇒	2.63	0.05	1.69
851.3	3			0.97	⇒			1.68

	4			0.96				1.67
	5			0.95				1.65

Similarly to the calculations performed for the previous studies, the data in Table 7 was used in Eq. (20) to calculate the muscle transmittance values, before and after the transparency treatment, and also to obtain the OC_{eff} of the E-cig in the muscle, using Eq. (21). Such calculated data is presented in Table 8.

Table 8 - Muscle transmittance of intensity-modulated laser before and after treatment with the E-cig solution and OC_{eff}.

λ (nm)	sample	T (%)	$\bar{T} \pm$ SD		T (%)	$\bar{T} \pm$ SD	$\overline{OC}_{eff} \pm$ SD
	1	0.820			6.557		
	2	0.820		⇒	6.557		
405.2	3	0.820	0.820 ± 0.00	⇒	7.377	7.377 ± 0.90	800.0 ± 110
	4	0.820		⇒	9.016		
	5	0.820			7.377		
	1	16.25			43.75		
	2	15.83		⇒	42.50		
520.4	3	15.83	16.50 ± 0.77	⇒	44.17	43.83 ± 0.81	166.2± 11.6
	4	16.67		⇒	45.00		
	5	17.92			43.75		
	1	21.52			50.42		
	2	22.78		⇒	50.84		
640.6	3	22.36	22.62 ± 0.63	⇒	50.42	50.67 ± 0.57	124.2 ± 6.06
	4	23.21		⇒	50.00		
	5	23.21			51.68		
	1	29.89			59.29		
	2	29.54		⇒	60.00		
782.0	3	31.67	30.75 ± 0.89	⇒	57.86	59.21 ± 0.80	92.78 ± 7.17
	4	30.96		⇒	58.93		
	5	31.67			60.00		
	1	34.00			62.67		
	2	34.33		⇒	62.33		
819.8	3	35.00	34.27 ± 0.39	⇒	61.33	61.73 ± 0.71	80.18 ± 3.09
	4	34.00		⇒	60.67		
	5	34.00			61.67		
	1	35.91			62.02		
	2	35.52		⇒	63.57		
851.3	3	35.52	35.37 ± 0.39	⇒	63.18	62.71 ± 0.62	77.34 ± 2.34
	4	35.14		⇒	62.79		
	5	34.75			62.02		

The data presented in Table 8 was used to create the graphs presented in Fig. 16, with the muscle transmittance at the laser wavelengths for the untreated and treated tissue is presented in Fig. 16(a), and the wavelength dependence of the OC_{eff} is presented in Fig. 16(b).

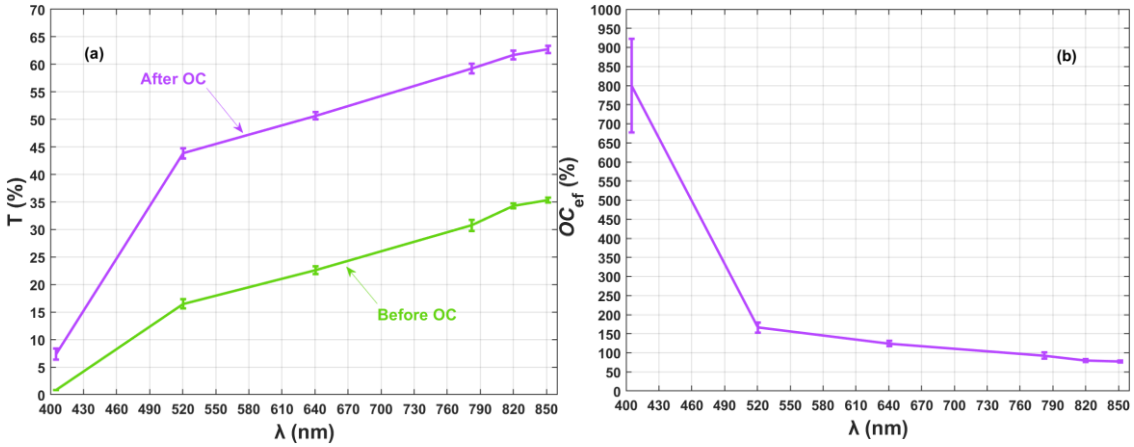

Figure 16 - Muscle transmittance as a function of laser wavelength before and after treatment with the E-cig fluid(a), and OC_{eff} as a function of laser wavelength.

The graphs presented in Fig. 16 show, once again, similar data to the one observed in the studies where the treatments with 64%-sucrose and 99%-glycerol were applied. The graphical data for the muscle transmittance that is presented in Fig. 16(a) shows that the transparency created by the E-cig fluid is somehow a little higher than the one created by the glycerol solution (see Fig. 15). This could be, since the propylene glycol in the E-cig fluid, which is hygroscopic, induces a fast and strong dehydration of the muscle at early treatment, allowing a bigger number of glycerol molecules from the solution to diffuse in to produce a higher RI matching mechanism [28], [35]. Fig. 16(b) helps in this analysis, since by eliminating the shape of the transmittance spectrum of the muscle samples, the OC_{eff} is a direct measurement of the impact of the OCA in the tissue and is well correlated to the efficiency of the RI matching mechanism that was induced. Indeed, comparing between the graphs in Figs. 15(b) and 16(b), we see higher OC_{eff} values for the treatment with E-cig. Such difference in the OC_{eff} values is observed for all laser wavelengths, showing that indeed, the treatment with E-cig leads to a higher efficiency of the RI matching mechanism in the spectral range considered in this research. These results show that by adding an hygroscopic agent to the treating solution, turns the initial dehydration mechanism faster, which facilitates the diffusion of a larger number of glycerol molecules to the inside of the tissue, even from a solution where its concentration is not too high.

4.3.4 Study of muscle transmittance before and after treatment with the 55%-TZ solution

To terminate the research, a final study was performed, where the muscle transmittance was evaluated from the untreated tissue, as well as after treatment with a solution containing 55% of TZ. Adopting the same experimental methodology as in the previous studies, the V_{pp} values measured at all laser wavelengths, that are required to calculate the muscle transmittance, are presented in Table 9.

Table 9 - Peak-to-peak voltage measurements before and after the OC treatment with the 55%-TZ solution.

λ (nm)	sample	$V_{pplaser}$ (V)	$V_{pp\text{-}noise}$ (V)	V_{pp} (V)		$V_{pplaser}$ (V)	$V_{pp\text{-}noise}$ (V)	V_{pp} (V)
	1			0.08				0.08
	2			0.07	⇒			0.08
405.2	3	1.32	0.05	0.07	⇒	1.30	0.05	0.08
	4			0.07	⇒			0.08
	5			0.07				0.08
	1			0.43				0.09
	2			0.43	⇒			0.07
520.4	3	2.45	0.05	0.44	⇒	2.47	0.05	0.07
	4			0.44	⇒			0.07
	5			0.46				0.07
	1			0.55				1.26
	2			0.58	⇒			1.32
640.6	3	2.42	0.05	0.57	⇒	2.43	0.05	1.36
	4			0.59	⇒			1.25
	5			0.60				1.28
	1			0.89				1.75
	2			0.90	⇒			1.72
782.0	3	2.86	0.05	0.92	⇒	2.83	0.05	1.74
	4			0.90	⇒			1.72
	5			0.91				1.73
	1			1.04				1.96
	2			1.05	⇒			1.95
819.8	3	3.05	0.05	1.03	⇒	3.05	0.05	1.96
	4			1.04	⇒			1.94
	5			1.02				1.93
	1			0.91				1.68
	2			0.93	⇒			1.70
851.3	3	2.63	0.05	0.94	⇒	2.63	0.05	1.71
	4			0.90	⇒			1.72
	5			0.93				1.71

The data in Table 9 was used to calculate the muscle transmittance at the laser wavelengths. Such calculations were performed with Eq. (20). Consequently, the calculated

transmittance values from the untreated and treated muscle samples were used in Eq. (21) to obtain the OC_{eff} for the treatment with the TZ solution. The results of these calculations are presented in Table 10.

Table 10 - Muscle transmittance of intensity-modulated laser before and after treatment with the 55%-TZ solution and OC_{eff}.

λ (nm)	sample	T (%)	$\overline{T} \pm$ SD		T (%)	$\overline{T} \pm$ SD	$\overline{OC}_{eff} \pm$ SD
	1	2.362			2.400		
	2	1.575		⇒	2.400		
405.2	3	1.575	1.732 ± 0.32	⇒	2.400	2.400 ± 0.00	42.24 ± 20.3
	4	1.575		⇒	2.400		
	5	1.575			2.400		
	1	15.83			1.653		
	2	15.83		⇒	0.826		
520.4	3	16.25	16.25 ± 0.46	⇒	0.826	0.992 ± 0.33	-93.87 ± 2.16
	4	16.25		⇒	0.826		
	5	17.08			0.826		
	1	21.10			50.84		
	2	22.36		⇒	53.36		
640.6	3	21.94	22.28 ± 0.73	⇒	55.04	52.27 ± 1.71	134.9 ± 11.3
	4	22.78		⇒	50.42		
	5	23.21			51.68		
	1	29.89			61.15		
	2	30.25		⇒	60.07		
782.0	3	30.96	30.39 ± 0.36	⇒	60.79	60.50 ± 0.42	99.11 ± 2.85
	4	30.25		⇒	60.07		
	5	30,60			60.43		
	1	33.00			63.67		
	2	33.33		⇒	63.33		
819.8	3	32.67	32.87 ± 0.34	⇒	63.46	63.18 ± 0.39	92.25 ± 1.78
	4	33.00		⇒	62.79		
	5	32.33			62.67		
	1	33.33			63.18		
	2	34.11		⇒	63.95		
851.3	3	34.50	33.80 ± 0.57	⇒	64.34	64.11 ± 0.53	89.73 ± 3.52
	4	32.95		⇒	64.73		
	5	34.11			64.34		

The data in Table 10 was represented graphically in Fig. 17, where the muscle transmittance, before and after treatment is seen in Fig. 17(a), and the OC_{eff} is seen in Fig. 17(b).

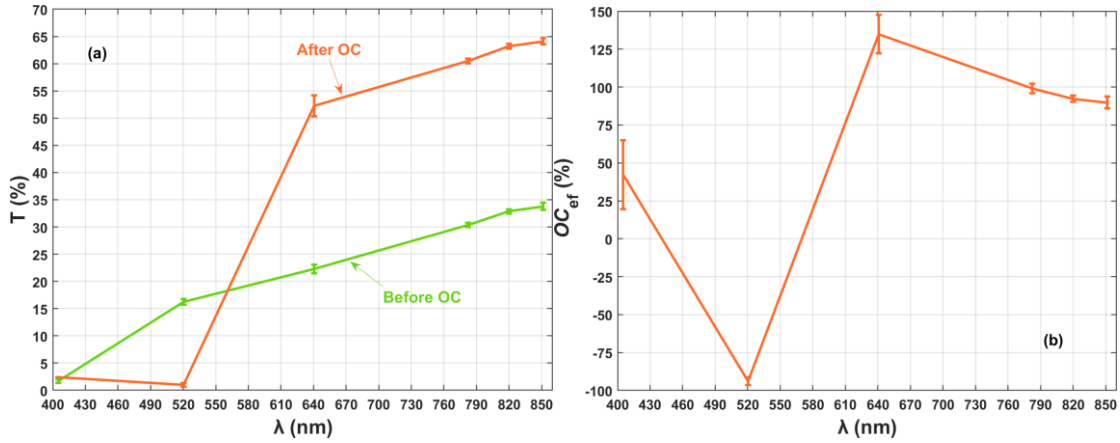

Figure 17 - Muscle transmittance as a function of laser wavelength before and after treatment with the 55%-TZ solution (a), and OC_{eff} as a function of laser wavelength.

Starting the analysis of the results presented in Fig. 17, we see that the wavelength dependence of muscle transmittance after treatment is different for the case where TZ is used as an OCA. Comparing between the two sets of data in Fig. 17(a), we see that although we observe a small increase in muscle transmittance at 405 nm, a strong decrease in muscle transmittance is observed at 520 nm, turning the muscle almost entirely opaque to light at that wavelength (nearly zero transmittance). Only for longer laser wavelengths we observe a similar behavior to those seen in the previous studies where tissues were treated with sucrose, glycerol and E-cig solutions. It is certain that the data presented in Fig. 17 is discrete, corresponding to the wavelengths of the lasers used to perform the measurements. Nevertheless, such data in Fig. 17(a) resembles the data presented in our recent paper, where kinetic and broadband spectroscopy measurements were performed from muscle samples under treatment with a solution containing 40% of TZ [86]. In that study it was also observed that muscle transparency only occurs for wavelengths longer than ~520 nm, as represented in Fig. 17(a). According to the explanation provided in that paper, the occurrence of an absorption band of TZ between 400 and 500 nm, with central peak at 436.36 nm as reported by Leulescu *et al.* [91], leads to the decrease of muscle transparency in a spectral range where the lasers with emission at 405 and 520 nm are located.

Considering now the OC_{eff} that is presented in Fig. 17(b), it is possible to confirm such interpretation of the TZ impact on the muscle. From that figure, we see that at 405 nm the OC_{eff} is approximately 40%. Such value is significantly smaller than the ones observed in the treatments performed with the other OCAs, but still positive. Moving to 520 nm, we see a negative efficiency, with a magnitude of ~100%, showing that at this wavelength the tissue

became significantly opaque to light due to the absorption band of TZ that occurs between 400 and 500 nm, as reported by Leulescu et al. [91]. The fact that such absorption band produces negative efficiency at 520 nm and positive efficiency at 405 nm is certainly related with the high concentration of TZ that was used in this study. The absorption band measured by Leulescu *et al.* was obtained from a solution with a TZ concentration lower than 5% [91], while in this study a solution containing 55% TZ was used. It is relevant to mention that, as reported by Leulescu *et al.*, TZ is a fluorescent food dye [91], and as indicated in our recent paper [86], as the TZ concentration in the treating solution increases, the effect of fluorescence changes the absorption bands. Such change in the absorption bands increases their magnitude and shifts their peaks, as we have recently studied at INESC TEC. Such study that shows a shift in the absorption bands to the longer wavelengths will be soon submitted to a journal for publication.

For longer wavelengths, 640 nm and higher, the OC_{eff} is significant and positive, showing a wavelength dependence similar to the one observed in the previous studies with the other OCAs. Such behavior is originated by the Lorentz-oscillator model, which shows that the fast decreasing slope of absorption bands leads to an optimized RI matching, as described by Ou *et. al.* [79]. Comparing between the graphs of OC_{eff} obtained for all the studies, we see that for wavelengths higher than 640 nm, the impact of TZ in the muscle is the highest, showing that such food dye is the best selection to create high magnitude transparency in muscle for the visible-NIR range.

4.3.5 Comparison of results between the treatments with different OCA solutions

To finalize this study, we will now perform a comparison between the transparency effects created by the four OCA solutions that were used. A first comparison was performed visually, by comparing photographs of the samples before and after the treatments, as represented in Fig. 18.

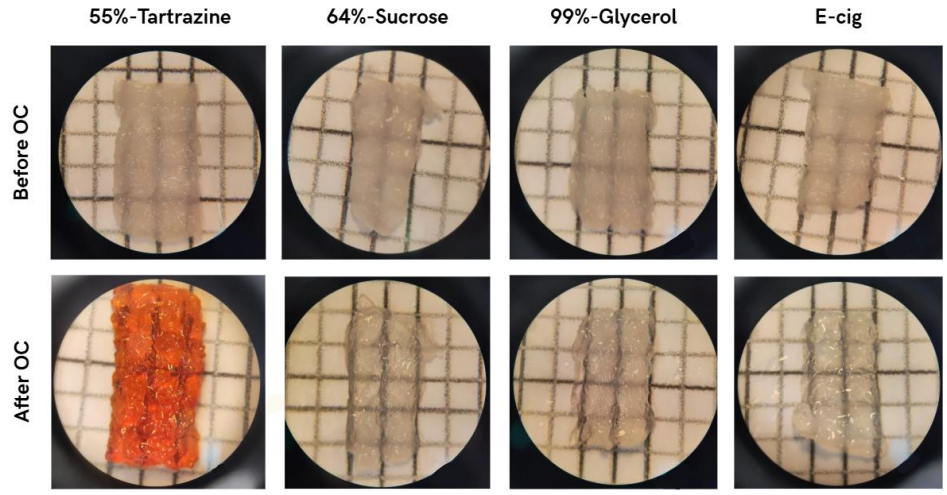

Figure 18 - Direct visual inspection of the samples before and after the different OC treatments.

The photographs presented in Fig. 18, show that after the OC treatment, all samples exhibit increased transparency, as indicated by the enhanced visibility of the underlying grid lines. This confirms that each agent contributed to some degree of optical clearing. The photographs from the tissues treated with the sucrose, glycerol and E-cig solutions show that the transparencies created by all these OCAs allow us to see the underlying grid with similarly good resolution. In the case of the treatment with TZ, the treated sample presents a reddish color, and the created transparency seems smaller than the one created by the other OCA solutions, providing a smaller resolution of the underlying grid in this case. Such result can be explained based on the analysis that we performed for the OC_{eff} that is presented in Fig. 17. As we saw in that graph, the transparency created by TZ shows negative efficiency for visible wavelengths lower than ~520 nm. Even if we consider spectral kinetic measurements, as presented in our recent paper [86], we see that the transparency created by a 40%-TZ solution increases very fast between 520 and 600 nm, showing only high magnitude transparency for longer wavelengths. This means that due to the occurrence of the absorption band of TZ between 400 and 500 nm, and through the Lorentz-oscillator model, transparency created by TZ only occurs for the visible spectral range between 600 and 720 nm. Once again, this result shows the good applicability of TZ to create transparency in the NIR spectral range. In opposition, the photographs from the samples treated with the other OCAs show no coloration and a good transparency in the entire visible range.

Considering the entire spectral range where the measurements with the intensity-modulated lasers were performed, a comparison between the magnitude of the transparencies created by each OCA solution can be made through Figs. 19 and 20.

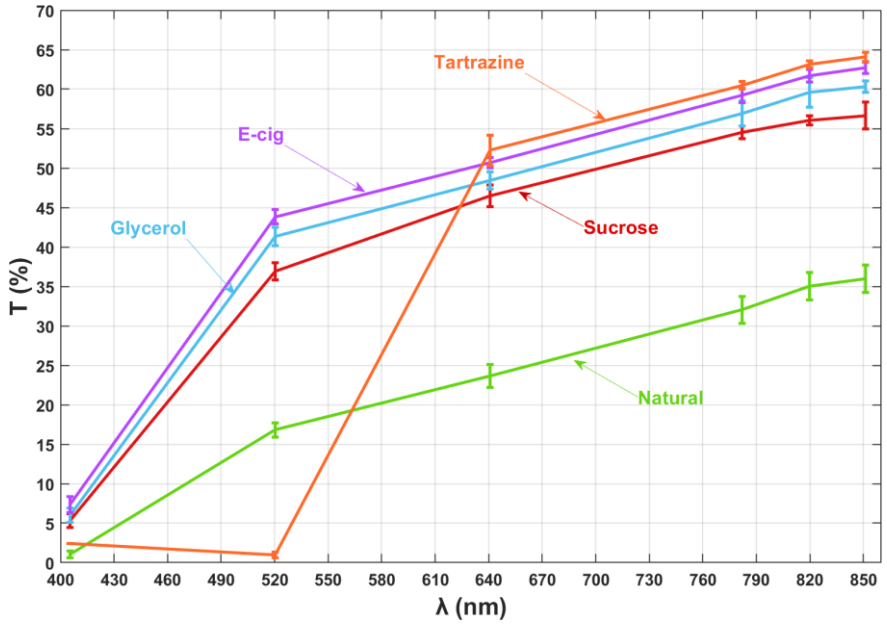

Figure 19 – Comparison of Transmittance results between the treatments with different OCA solutions.

By presenting all transmittance data that were collected from the various studies in one figure, it becomes simple to perform a comparison. From Fig. 19, we see that TZ is the OCA that creates high magnitude transparency, but only for wavelengths ≥ 640 nm. Considering the other OCAs, E-cig provides the highest transparency in the entire spectral range, followed by glycerol and then sucrose.

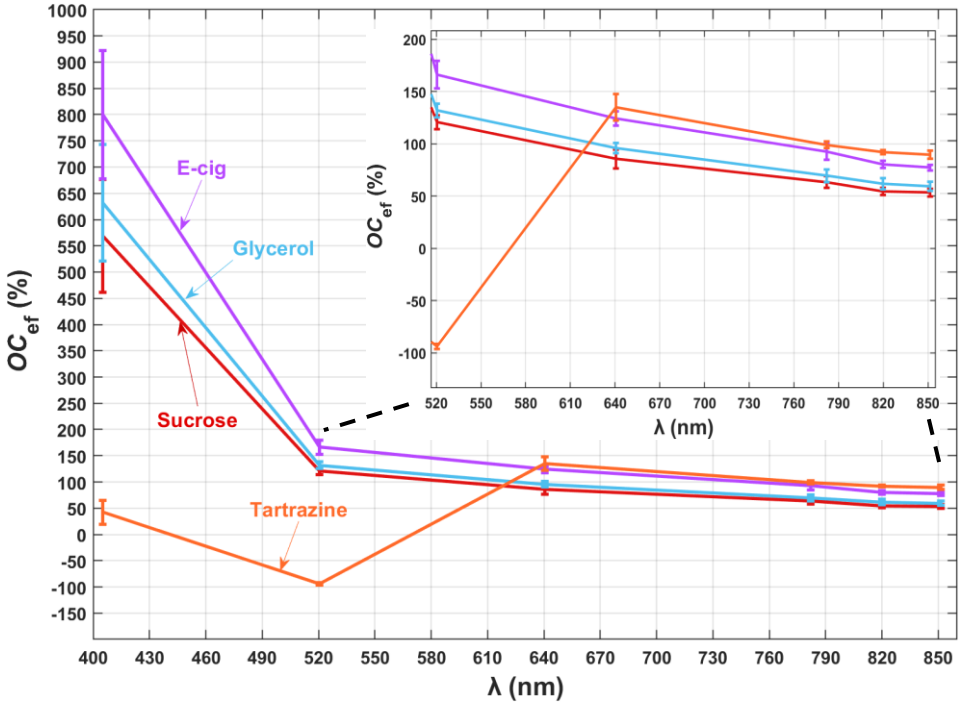

Figure 20 - Comparison of OC_{eff} results between the treatments with different OCA solutions.

The OC_{eff} data presented in Fig. 20 allows a direct comparison between the impact of the various OCAs in the muscle, as well as to infer the dependence between the efficiency of the RI matching mechanism with wavelength that occurs in each treatment. From this figure, we see that sucrose is the OCA that presents the lowest OC_{eff} values for all laser wavelengths, with the exception of TZ at 405 and 520 nm, for the reasons already explained. Glycerol presents intermediate efficiency values for all wavelengths, while E-cig is the OCA that induces the highest transparency in the muscle. These results proof the importance of combining a hygroscopic agent, as propylene glycol, with an OCA, such as glycerol, which was used in E-cig. Such combination prevents the diffusion of the OCA into the tissue to occur simultaneously and in opposite direction to the water flux out, which slows the OCA diffusion into the tissue [101].

For wavelengths equal of longer than 640 nm, TZ presents an efficiency a little higher than E-cig. Such fact shows that TZ is able to create high transparency in muscle in the visible-NIR range, but to avoid the decrease of natural transparency at lower visible wavelengths, E-cig can be used to produce a similar effect at longer wavelengths. Possibly, solutions with even higher concentrations of TZ can produce bigger transparency in muscle, but the physiological impact of such highly-concentrated TZ solutions in tissues needs to be evaluated first. It has been referred that TZ bonds to DNA and interacts with proteins [91], so these and other physiological interactions of TZ as a function of TZ concentration in solution need urgent evaluation.

As a final result from Fig. 20, it should be mentioned that with the exception of TZ, the other OCAs present their highest efficiency values at 405 nm, showing that the RI matching mechanism is more efficient at lower wavelengths. Although the lasers used in the present study correspond only to the visible-NIR range, the results here obtained suggest that higher magnitude transparency effects can be obtained in the UV, as a consequence of an even higher efficiency of the RI matching mechanism in a spectral range where tissues present high scattering properties.

Chapter 5 – Conclusion

5 Conclusion

The present study was conducted with the objective to evaluate the transmittance of intensity-modulated laser beans in muscle and how it can improve with the creation of transparency effects. Six lasers and four OCA solutions were selected to conduct this study, allowing the comparison between the obtained results with the four OCA solutions and as a function of wavelength, in the visible-NIR spectral range. Although the experiments did not use an optimized setup to measure the collimated transmittance of the muscle samples with the lasers, it was possible to verify that the applied treatments induced a higher transmittance of the muscle for the various laser wavelengths. Such effect was only partially verified for the treatment with the TZ solution, since due to the existence of an absorption band of this food dye between 400 and 500 nm, the improvement in tissue transparency was only observed for wavelengths longer than 520 nm. It was also observed that the efficiency of the 55%-TZ solution in creating transparency in the muscle is similar to the one obtained with the E-cig solution for longer wavelengths. Such similar results suggest that an even higher efficiency can be obtained with the use of TZ in solutions with higher concentrations, but such solutions might induce undesirable physiological effects in the tissues. Considering the data obtained in this study as a function of wavelength, and with the exception of the treatment with the TZ solution, it was verified that the various OCAs induce a higher magnitude RI matching between the ISF and the scatterers of the muscle at lower wavelengths, where the scattering properties of the tissues are stronger. Such results are consistent with previous studies that report the creation of UV transparency windows in tissues with high magnitude. Further studies with UV lasers are required to take advantage of such transparency windows for the development of innovative diagnostic and treatment protocols based on the use of light.

Although the present study was conducted with skeletal muscle samples, similar studies with other tissues are required due to the different physiological conditions that the various tissue present, which might condition the transparency created by the various OCAs. Additionally, other OCAs should be used in those studies, as well as other lasers that operate at other wavelengths, such as the UV. The absorption and interaction of lasers with DNA and proteins is highly interesting nowadays, and studies with lasers emitting in the UV-C range can provide information about such interactions, when combined with

temporary transparency effects. Considering the study with TZ, studies with other absorbing molecules, such as hemoglobin and other food dyes are also interesting to create transparency, since due to the Lorentz-oscillator model, transparency can be created in selectable spectral ranges for particular Biophotonics applications.

6 References

[1] A. J. Nanavati and S. Nagral, “Why have we embraced minimally invasive surgery and ignored enhanced recovery after surgery?,” *J. Minimal Access Surg.*, vol. 12, no. 3, pp. 299–301, 2016, doi: 10.4103/0972-9941.181392.

[2] M. Michalik, J. Szymańczyk, M. Stajnke, T. Ochrymiuk, and A. Cenian, “Medical Applications of Diode Lasers: Pulsed versus Continuous Wave (cw) Regime,” *Micromachines*, vol. 12, no. 6, p. 710, Jun. 2021, doi: 10.3390/mi12060710.

[3] B. W. Pogue, “Perspective on the optics of medical imaging,” *J. Biomed. Opt.*, vol. 28, no. 12, p. 121208, Dec. 2023, doi: 10.1117/1.JBO.28.12.121208.

[4] Y. Puckett, Y. A. Al-Naser, and T. M. Nappe, “Ionizing Radiation,” in *StatPearls*, Treasure Island (FL): StatPearls Publishing, 2025. Accessed: Mar. 27, 2025. [Online]. Available: http://www.ncbi.nlm.nih.gov/books/NBK534237/

[5] A. N. Pereira, C. de P. Eduardo, E. Matson, and M. M. Marques, “Effect of low-power laser irradiation on cell growth and procollagen synthesis of cultured fibroblasts,” *Lasers Surg. Med.*, vol. 31, no. 4, pp. 263–267, 2002, doi: 10.1002/lsm.10107.

[6] T. S. Kim *et al.*, “9.4 MHz A-line rate optical coherence tomography at 1300 nm using a wavelength-swept laser based on stretched-pulse active mode-locking,” *Sci. Rep.*, vol. 10, no. 1, p. 9328, Jun. 2020, doi: 10.1038/s41598-020-66322-0.

[7] S. Farivar, T. Malekshahabi, and R. Shiari, “Biological effects of low level laser therapy,” *J. Lasers Med. Sci.*, vol. 5, no. 2, pp. 58–62, 2014.

[8] D. Hawkins, N. Houreld, and H. Abrahamse, “Low Level Laser Therapy (LLLT) as an Effective Therapeutic Modality for Delayed Wound Healing,” *Ann. N. Y. Acad. Sci.*, vol. 1056, no. 1, pp. 486–493, 2005, doi: 10.1196/annals.1352.040.

[9] R. J. Lanzafame, “Laser/Light Applications in General Surgery,” in *Lasers in Dermatology and Medicine: Dental and Medical Applications*, K. Nouri, Ed., Cham: Springer International Publishing, 2018, pp. 135–162. doi: 10.1007/978-3-319-76220-3_7.

[10] S. Teymour, B. Kania, K. Lal, and D. Goldberg, “Energy-based devices in the treatment of acne scars in skin of color,” *J. Cosmet. Dermatol.*, vol. 22, no. 4, pp. 1177–1184, Apr. 2023, doi: 10.1111/jocd.15572.

[11] B. Považay, R. Brinkmann, M. Stoller, and R. Kessler, “Selective Retina Therapy,” in *High Resolution Imaging in Microscopy and Ophthalmology: New Frontiers in Biomedical Optics*, J. F. Bille, Ed., Cham (CH): Springer, 2019. Accessed: Mar. 27, 2025. [Online]. Available: http://www.ncbi.nlm.nih.gov/books/NBK554033/

[12] A. M. Luke, S. Mathew, M. M. Altawash, and B. M. Madan, “Lasers: A Review With Their Applications in Oral Medicine,” *J. Lasers Med. Sci.*, vol. 10, no. 4, pp. 324–329, 2019, doi: 10.15171/jlms.2019.52.

[13] S. Taha, W. R. Mohamed, M. A. Elhemely, A. O. El-Gendy, and T. Mohamed, "Tunable femtosecond laser suppresses the proliferation of breast cancer in vitro," *J. Photochem. Photobiol. B*, vol. 240, p. 112665, Mar. 2023, doi: 10.1016/j.jphotobiol.2023.112665.

[14] C. for D. and R. Health, "Medical Lasers," *FDA*, Feb. 2023, Accessed: Mar. 27, 2025. [Online]. Available: https://www.fda.gov/radiation-emitting-products/surgical-and-therapeutic-products/medical-lasers

[15] Q. Peng *et al.*, "Lasers in medicine," *Rep. Prog. Phys.*, vol. 71, no. 5, p. 056701, Apr. 2008, doi: 10.1088/0034-4885/71/5/056701.

[16] B. Pajic, B. Pajic-Eggspuehler, C. Rathjen, M. Resan, and Z. Cvejic, "Why Use Ultrashort Pulses in Ophthalmology and Which Factors Affect Cut Quality," *Med. Kaunas Lith.*, vol. 57, no. 7, p. 700, Jul. 2021, doi: 10.3390/medicina57070700.

[17] R. Lanzafame, "Light Dosing and Tissue Penetration: It Is Complicated," *Photobiomodulation Photomed. Laser Surg.*, vol. 38, no. 7, pp. 393–394, Jul. 2020, doi: 10.1089/photob.2020.4843.

[18] S. L. Jacques, "Optical properties of biological tissues: a review," *Phys. Med. Biol.*, vol. 58, no. 11, pp. R37-61, Jun. 2013, doi: 10.1088/0031-9155/58/11/R37.

[19] V. V. Tuchin, *Tissue Optics: Light Scattering Methods and Instruments for Medical Diagnosis*. Society of Photo-Optical Instrumentation Engineers (SPIE), 2015. doi: 10.1117/3.1003040.

[20] I. Carneiro, S. Carvalho, R. Henrique, L. Oliveira, and V. Tuchin, "Moving tissue spectral window to the deep-ultraviolet via optical clearing," *J. Biophotonics*, vol. 12, no. 12, p. e201900181, Dec. 2019, doi: 10.1002/jbio.201900181.

[21] I. S. Martins *et al.*, "Measurement of tissue optical properties in a wide spectral range: a review [Invited]," *Biomed. Opt. Express*, vol. 14, no. 1, pp. 249–298, Jan. 2023, doi: 10.1364/BOE.479320.

[22] M. R. Pinheiro, M. I. Carvalho, and L. M. Oliveira, "Tutorial on the Use of the Photon Diffusion Approximation for Fast Calculation of Tissue Optical Properties," *J. Biophotonics*, p. e202400257, Oct. 2024, doi: 10.1002/jbio.202400257.

[23] D. Siposan, "19 - Lasers in neurology," in *Lasers for Medical Applications*, H. Jelínková, Ed., in Woodhead Publishing Series in Electronic and Optical Materials. , Woodhead Publishing, 2013, pp. 573–603. doi: 10.1533/9780857097545.4.573.

[24] S. Marasini, S. J. Dean, S. Swift, and J. P. Craig, "Comparison of antimicrobial efficacy and safety of pulsed versus continuous wave UVC," *Contact Lens Anterior Eye J. Br. Contact Lens Assoc.*, p. 102437, May 2025, doi: 10.1016/j.clae.2025.102437.

[25] T. Li *et al.*, "Transcranial photobiomodulation induced frequency-specific dual-pathway glial activation for neurovascular protection vs amyloid clearance in Alzheimer's disease," Jun. 19, 2025, *Research Square*. doi: 10.21203/rs.3.rs-6906760/v1.

[26] L. M. C. Oliveira and V. V. Tuchin, *The Optical Clearing Method: A New Tool for Clinical Practice and Biomedical Engineering*. in SpringerBriefs in Physics. Cham: Springer International Publishing, 2019. doi: 10.1007/978-3-030-33055-2.

[27] S. Carvalho, N. Gueiral, E. Nogueira, R. Henrique, L. Oliveira, and V. V. Tuchin, "Glucose diffusion in colorectal mucosa-a comparative study between normal and cancer tissues," *J. Biomed. Opt.*, vol. 22, no. 9, p. 91506, Sep. 2017, doi: 10.1117/1.JBO.22.9.091506.

[28] L. R. Oliveira, R. M. Ferreira, M. R. Pinheiro, H. F. Silva, V. V. Tuchin, and L. M. Oliveira, "Broadband spectral verification of optical clearing reversibility in lung tissue," *J. Biophotonics*, vol. 16, no. 1, p. e202200185, Jan. 2023, doi: 10.1002/jbio.202200185.

[29] M. R. Pinheiro, V. V. Tuchin, and L. M. Oliveira, "Invasive and Minimally Invasive Evaluation of Diffusion Properties of Sugar in Muscle," *IEEE J. Sel. Top. Quantum Electron.*, vol. 29, no. 4: Biophotonics, pp. 1–8, Jul. 2023, doi: 10.1109/JSTQE.2023.3255801.

[30] L. Oliveira, I. Carneiro, S. Carvalho, R. Henrique, and V. Tuchin, "Método de criação de janelas óticas de diagnóstico e tratamento em materiais biológicos na zona do ultravioleta," 2020, Accessed: Mar. 28, 2025. [Online]. Available: http://hdl.handle.net/10400.22/17928

[31] Y. Zhou, J. Yao, and L. V. Wang, "Tutorial on photoacoustic tomography," *J. Biomed. Opt.*, vol. 21, no. 6, p. 61007, Jun. 2016, doi: 10.1117/1.JBO.21.6.061007.

[32] S. Peña-Llopis and J. Brugarolas, "Simultaneous isolation of high-quality DNA, RNA, miRNA and proteins from tissues for genomic applications," *Nat. Protoc.*, vol. 8, no. 11, pp. 2240–2255, Nov. 2013, doi: 10.1038/nprot.2013.141.

[33] M. R. Pinheiro *et al.*, "Optimized reconstruction of the absorption spectra of kidney tissues from the spectra of tissue components using the least squares method," *J. Biophotonics*, p. e202300466, Feb. 2024, doi: 10.1002/jbio.202300466.

[34] I. Carneiro, S. Carvalho, R. Henrique, A. Selifonov, L. Oliveira, and V. V. Tuchin, "Enhanced Ultraviolet Spectroscopy by Optical Clearing for Biomedical Applications," *IEEE J. Sel. Top. Quantum Electron.*, vol. 27, no. 4, pp. 1–8, Jul. 2021, doi: 10.1109/JSTQE.2020.3012350.

[35] V. V. Tuchin, D. Zhu, and E. A. Genina, Eds., *Handbook of Tissue Optical Clearing: New Prospects in Optical Imaging*. Boca Raton: CRC Press, 2022. doi: 10.1201/9781003025252.

[36] S. P. Power, F. Moloney, M. Twomey, K. James, O. J. O'Connor, and M. M. Maher, "Computed tomography and patient risk: Facts, perceptions and uncertainties," *World J. Radiol.*, vol. 8, no. 12, pp. 902–915, Dec. 2016, doi: 10.4329/wjr.v8.i12.902.

[37] P. Matryba, L. Kaczmarek, and J. Gołąb, "Advances in Ex Situ Tissue Optical Clearing," *Laser Photonics Rev.*, vol. 13, no. 8, p. 1800292, 2019, doi: 10.1002/lpor.201800292.

[38] A. J. M. Wollman, R. Nudd, E. G. Hedlund, and M. C. Leake, "From Animaculum to single molecules: 300 years of the light microscope," *Open Biol.*, vol. 5, no. 4, p. 150019, Apr. 2015, doi: 10.1098/rsob.150019.

[39] R. Splinter and B. A. Hooper, *An Introduction to Biomedical Optics*. Boca Raton: CRC Press, 2006. doi: 10.1201/9781420011838.

[40] Y. Zhou *et al.*, "Human brain cancer studied by resonance Raman spectroscopy," *J. Biomed. Opt.*, vol. 17, no. 11, p. 116021, Nov. 2012, doi: 10.1117/1.JBO.17.11.116021.

[41] B. S. Deo, S. Nayak, M. Pal, P. K. Panigrahi, and A. Pradhan, "Empirical mode decomposition and Hessian LLE in Fluorescence spectral signal analysis for Cervical cancer detection," *Biomed. Signal Process. Control*, vol. 100, p. 106917, Feb. 2025, doi: 10.1016/j.bspc.2024.106917.

[42] M. Shur, "Terahertz sensing and imaging technology of cancer detection," in *Terahertz, RF, Millimeter, and Submillimeter-Wave Technology and Applications XVIII*, SPIE, Mar. 2025, pp. 90–96. doi: 10.1117/12.3048619.

[43] D. Schwartz, T. W. Sawyer, N. Thurston, J. Barton, and G. Ditzler, "Ovarian cancer detection using optical coherence tomography and convolutional neural networks," *Neural Comput. Appl.*, vol. 34, no. 11, pp. 8977–8987, Jun. 2022, doi: 10.1007/s00521-022-06920-3.

[44] E. HASE, T. MINAMIKAWA, K. SATO, D. YONEKURA, M. TAKAHASHI, and T. YASUI, "Observation of Tendon Healing with Second-harmonic-generation (SHG) Microscopy," *Trans. Jpn. Soc. Med. Biol. Eng.*, vol. 54, no. 6, pp. 253–260, 2016, doi: 10.11239/jsmbe.54.253.

[45] M. M. Qureshi, Y. Liu, K. D. Mac, M. Kim, A. M. Safi, and E. Chung, "Quantitative blood flow estimation in vivo by optical speckle image velocimetry," *Optica*, vol. 8, no. 8, pp. 1092–1101, Aug. 2021, doi: 10.1364/OPTICA.422871.

[46] B. Azadgoli and R. Y. Baker, "Laser applications in surgery," *Ann. Transl. Med.*, vol. 4, no. 23, p. 452, Dec. 2016, doi: 10.21037/atm.2016.11.51.

[47] D. R. Paschotta, "Pulsed Lasers," *RP Photonics Encycl.*, Nov. 2005, Accessed: Jun. 16, 2025. [Online]. Available: https://www.rp-photonics.com/pulsed_lasers.html

[48] D. R. Paschotta, "Pulse Trains," *RP Photonics Encycl.*, Mar. 2021, Accessed: Jun. 16, 2025. [Online]. Available: https://www.rp-photonics.com/pulse_trains.html

[49] R. A. Mussttaf, D. F. L. Jenkins, and A. N. Jha, "Assessing the impact of low level laser therapy (LLLT) on biological systems: a review," *Int. J. Radiat. Biol.*, vol. 95, no. 2, pp. 120–143, Feb. 2019, doi: 10.1080/09553002.2019.1524944.

[50] S. Yang *et al.*, "Femtosecond laser lithotripsy: a novel alternative for kidney stone treatment? Evaluating the safety and effectiveness in an ex vivo study," *Urolithiasis*, vol. 51, no. 1, p. 118, Oct. 2023, doi: 10.1007/s00240-023-01493-9.

[51] I. Viozzi, A. Guberinic, C. G. Overduin, M. M. Rovers, and M. Ter Laan, "Laser Interstitial Thermal Therapy in Patients with Newly Diagnosed Glioblastoma: A Systematic Review," *J. Clin. Med.*, vol. 10, no. 2, p. 355, Jan. 2021, doi: 10.3390/jcm10020355.

[52] R. L. Siegel, K. D. Miller, H. E. Fuchs, and A. Jemal, “Cancer statistics, 2022,” *CA. Cancer J. Clin.*, vol. 72, no. 1, pp. 7–33, Jan. 2022, doi: 10.3322/caac.21708.

[53] D. R. Risbridger *et al.*, “Novel optical technologies for ultrashort pulsed laser surgery: European Conferences on Biomedical Optics 2019,” *Nov. Biophotonics Tech. Appl. V*, Jul. 2019, doi: 10.1117/12.2527081.

[54] A. A. Ebid and A. M. El-Sodany, “Long-term effect of pulsed high-intensity laser therapy in the treatment of post-mastectomy pain syndrome: a double blind, placebo-control, randomized study,” *Lasers Med. Sci.*, vol. 30, no. 6, pp. 1747–1755, Aug. 2015, doi: 10.1007/s10103-015-1780-z.

[55] A. Consales *et al.*, “Magnetic Resonance-Guided Laser Interstitial Thermal Therapy (MR-gLiTT) in Pediatric Epilepsy Surgery: State of the Art and Presentation of Giannina Gaslini Children’s Hospital (Genoa, Italy) Series,” *Front. Neurol.*, vol. 12, p. 739034, 2021, doi: 10.3389/fneur.2021.739034.

[56] I. F. Naterstad, J. Joensen, J. M. Bjordal, C. Couppé, R. A. B. Lopes-Martins, and M. B. Stausholm, “Efficacy of low-level laser therapy in patients with lower extremity tendinopathy or plantar fasciitis: systematic review and meta-analysis of randomised controlled trials,” *BMJ Open*, vol. 12, no. 9, p. e059479, Sep. 2022, doi: 10.1136/bmjopen-2021-059479.

[57] O. Vazquez-Martinez *et al.*, “Pulsed Dye Laser for Early Treatment of Scars After Dermatological Surgery,” *J. Drugs Dermatol. JDD*, vol. 14, no. 11, pp. 1209–1212, Nov. 2015.

[58] C. Geldi, O. Bozkulak, H. O. Tabakoglu, S. Isci, A. Kurt, and M. Gulsoy, “Development of a surgical diode-laser system: controlling the mode of operation,” *Photomed. Laser Surg.*, vol. 24, no. 6, pp. 723–729, Dec. 2006, doi: 10.1089/pho.2006.24.723.

[59] K. Maslov and L. V. Wang, “Photoacoustic imaging of biological tissue with intensity-modulated continuous-wave laser,” *J. Biomed. Opt.*, vol. 13, no. 2, p. 024006, 2008, doi: 10.1117/1.2904965.

[60] L. Baratto, R. Capra, M. Farinelli, P. Monteforte, P. Morasso, and G. Rovetta, “A new type of very low-power modulated laser: soft-tissue changes induced in osteoarthritic patients revealed by sonography,” *Int. J. Clin. Pharmacol. Res.*, vol. 20, no. 1–2, pp. 13–16, 2000.

[61] M. Inyushin, D. Meshalkina, L. Zueva, and A. Zayas-Santiago, “Tissue Transparency In Vivo,” *Molecules*, vol. 24, no. 13, Art. no. 13, Jan. 2019, doi: 10.3390/molecules24132388.

[62] N. M. Gomes, V. V. Tuchin, and L. M. Oliveira, “Refractive Index Matching Efficiency in Colorectal Mucosa Treated With Glycerol,” *IEEE J. Sel. Top. Quantum Electron.*, vol. 27, no. 4, pp. 1–8, Jul. 2021, doi: 10.1109/JSTQE.2021.3050208.

[63] V. V. Tuchin, I. L. Maksimova, D. A. Zimnyakov, I. L. Kon, A. H. Mavlyutov, and A. A. Mishin, “Light propagation in tissues with controlled optical properties,” *J. Biomed. Opt.*, vol. 2, no. 4, pp. 401–417, Oct. 1997, doi: 10.1117/12.281502.

[64] V. V. Tuchin and L. Oliveira, “Recent progress in tissue enhanced spectroscopy for cancer detection,” 2021, Accessed: Apr. 23, 2025. [Online]. Available: http://hdl.handle.net/10400.22/20019

[65] A. Yu. Sdobnov, M. E. Darvin, E. A. Genina, A. N. Bashkatov, J. Lademann, and V. V. Tuchin, “Recent progress in tissue optical clearing for spectroscopic application,” *Spectrochim. Acta. A. Mol. Biomol. Spectrosc.*, vol. 197, pp. 216–229, May 2018, doi: 10.1016/j.saa.2018.01.085.

[66] J. Rheims, J. Köser, and T. Wriedt, “Refractive-index measurements in the near-IR using an Abbe refractometer,” *Meas. Sci. Technol.*, vol. 8, no. 6, p. 601, Jun. 1997, doi: 10.1088/0957-0233/8/6/003.

[67] C. Choe, J. Lademann, and M. E. Darvin, “Depth profiles of hydrogen bound water molecule types and their relation to lipid and protein interaction in the human stratum corneum in vivo,” *Analyst*, vol. 141, no. 22, pp. 6329–6337, Oct. 2016, doi: 10.1039/C6AN01717G.

[68] A. Y. Sdobnov, M. E. Darvin, J. Schleusener, J. Lademann, and V. V. Tuchin, “Hydrogen bound water profiles in the skin influenced by optical clearing molecular agents—Quantitative analysis using confocal Raman microscopy,” *J. Biophotonics*, vol. 12, no. 5, p. e201800283, 2019, doi: 10.1002/jbio.201800283.

[69] M. A. Saraiva, “Interpretation of α-synuclein UV absorption spectra in the peptide bond and the aromatic regions,” *J. Photochem. Photobiol. B*, vol. 212, p. 112022, Nov. 2020, doi: 10.1016/j.jphotobiol.2020.112022.

[70] A. T. Yeh, B. Choi, J. S. Nelson, and B. J. Tromberg, “Reversible dissociation of collagen in tissues,” *J. Invest. Dermatol.*, vol. 121, no. 6, pp. 1332–1335, Dec. 2003, doi: 10.1046/j.1523-1747.2003.12634.x.

[71] J. M. Hirshburg, K. M. Ravikumar, W. Hwang, and A. T. Yeh, “Molecular basis for optical clearing of collagenous tissues,” *J. Biomed. Opt.*, vol. 15, no. 5, p. 055002, Sep. 2010, doi: 10.1117/1.3484748.

[72] J. Wang, N. Ma, R. Shi, Y. Zhang, T. Yu, and D. Zhu, “Sugar-Induced Skin Optical Clearing: From Molecular Dynamics Simulation to Experimental Demonstration,” *IEEE J. Sel. Top. Quantum Electron.*, vol. 20, no. 2, pp. 256–262, Mar. 2014, doi: 10.1109/JSTQE.2013.2289966.

[73] W. Spalteholz, *Über das Durchsichtigmachen von menschlichen und tierischen Präparaten und seine theoretischen Bedingungen, nebst Anhang: Über Knochenfärbung*. S. Hirzel, 1911.

[74] W. Spalteholz, *Über das Durchsichtigmachen von menschlichen und tierischen Präparaten und seine theoretischen Bedingungen, nebst Anhang: Über Knochenfärbung*. S. Hirzel, 1914.

[75] D. K. Tuchina *et al.*, “Ex vivo optical measurements of glucose diffusion kinetics in native and diabetic mouse skin,” *J. Biophotonics*, vol. 8, no. 4, pp. 332–346, 2015, doi: 10.1002/jbio.201400138.

[76] S. M. Zaytsev, M. Amouroux, V. V. Tuchin, E. A. Genina, and W. Blondel, “In vivo skin optical clearing efficacy quantification of clinically compatible agents using line-field confocal optical coherence tomography,” *J. Biomed. Opt.*, vol. 28, no. 5, p. 055002, May 2023, doi: 10.1117/1.JBO.28.5.055002.

[77] G. T. Franzesi *et al.*, “In Vivo Optical Clearing of Mammalian Brain,” Sep. 11, 2024, *bioRxiv*. doi: 10.1101/2024.09.05.611421.

[78] A. Banerjee, A. Indoliya, and R. Poddar, “Edible oil based optical clearing for optical coherence tomography angiography imaging,” *Microvasc. Res.*, vol. 154, p. 104671, Jul. 2024, doi: 10.1016/j.mvr.2024.104671.

[79] Z. Ou *et al.*, “Achieving optical transparency in live animals with absorbing molecules,” *Science*, vol. 385, no. 6713, p. eadm6869, Sep. 2024, doi: 10.1126/science.adm6869.

[80] I. Grzelewska-Rzymowska, M. Szmidt, M. L. Kowalski, and J. Roźniecki, “Sensitivity and tolerance to tartrazine in aspirin-sensitive asthmatics,” *Allergol. Immunopathol. (Madr.)*, vol. 14, no. 1, pp. 31–36, 1986.

[81] E. H. Corder and C. E. Buckley, “Aspirin, salicylate, sulfite and tartrazine induced bronchoconstriction. Safe doses and case definition in epidemiological studies,” *J. Clin. Epidemiol.*, vol. 48, no. 10, pp. 1269–1275, Oct. 1995, doi: 10.1016/0895-4356(95)00017-X.

[82] N. H. Choulis, “49 - Miscellaneous drugs, materials, medical devices, and techniques,” in *Side Effects of Drugs Annual*, vol. 32, J. K. Aronson, Ed., in Side Effects of Drugs Annual 32, vol. 32. , Elsevier, 2010, pp. 891–902. doi: 10.1016/S0378-6080(10)32049-6.

[83] D. D. Thanh *et al.*, “The food dye Tartrazine disrupts vascular formation both in zebrafish larvae and in human primary endothelial cells,” *Sci. Rep.*, vol. 14, no. 1, p. 30367, Dec. 2024, doi: 10.1038/s41598-024-82076-5.

[84] J. Ma, B. Chen, Y. Zhang, D. Li, and Z. L. Xing, “Multiple laser pulses in conjunction with an optical clearing agent to improve the curative effect of cutaneous vascular lesions,” *Lasers Med. Sci.*, vol. 32, no. 6, pp. 1321–1335, Aug. 2017, doi: 10.1007/s10103-017-2244-4.

[85] B. Shariati B. K., M. A. Ansari, S. S. Khatami, and V. V. Tuchin, “Multimodal optical clearing to minimize light attenuation in biological tissues,” *Sci. Rep.*, vol. 13, no. 1, p. 21509, Dec. 2023, doi: 10.1038/s41598-023-48876-x.

[86] A. R. Guerra *et al.*, “Tartrazine for Optical Clearing of Tissues: Stability and Diffusion Issues,” *J. Biophotonics*, p. e202500160, Jul. 2025, doi: 10.1002/jbio.202500160.

[87] I. Carneiro, S. Carvalho, R. Henrique, L. Oliveira, and V. V. Tuchin, “Kinetics of Optical Properties of Colorectal Muscle During Optical Clearing,” *IEEE J. Sel. Top. Quantum Electron.*, vol. 25, no. 1, pp. 1–8, Jan. 2019, doi: 10.1109/JSTQE.2018.2840346.

[88] I. S. Martins, H. F. Silva, V. V. Tuchin, and L. M. Oliveira, “Fast Estimation of the Spectral Optical Properties of Rabbit Pancreas and Pigment Content Analysis,” *Photonics*, vol. 9, no. 2, Art. no. 2, Feb. 2022, doi: 10.3390/photonics9020122.

[89] S. Carvalho, I. Carneiro, R. Henrique, V. Tuchin, and L. Oliveira, “Lipofuscin-Type Pigment as a Marker of Colorectal Cancer,” *Electronics*, vol. 9, no. 11, Art. no. 11, Nov. 2020, doi: 10.3390/electronics9111805.

[90] L. R. Oliveira, M. R. Pinheiro, D. K. Tuchina, P. A. Timoshina, M. I. Carvalho, and L. M. Oliveira, “Light in evaluation of molecular diffusion in tissues: Discrimination of pathologies,” *Adv. Drug Deliv. Rev.*, vol. 212, p. 115420, Sep. 2024, doi: 10.1016/j.addr.2024.115420.

[91] M. Leulescu *et al.*, “Tartrazine: physical, thermal and biophysical properties of the most widely employed synthetic yellow food-colouring azo dye,” *J. Therm. Anal. Calorim.*, vol. 134, no. 1, pp. 209–231, Oct. 2018, doi: 10.1007/s10973-018-7663-3.

[92] R. D. Birkhoff, L. R. Painter, and J. M. Heller Jr., “Optical and dielectric functions of liquid glycerol from gas photoionization measurements,” *J. Chem. Phys.*, vol. 69, no. 9, pp. 4185–4188, Nov. 1978, doi: 10.1063/1.437098.

[93] B. A and A. G, “Concentration, Wavelength and Temperature Dependent Refractive Index of Sugar Solutions and Methods of Determination Contents of Sugar in Soft Drink Beverages using Laser Lights,” *J. Lasers Opt. Photonics*, vol. 05, no. 02, 2018, doi: 10.4172/2469-410X.1000187.

[94] D. Jakubczyk, G. Derkachov, K. Nyandey, S. Alikhanzadeh-Arani, and A. Derkachova, “Chromatic dispersion and thermal coefficients of hygroscopic liquids: 5 glycols and glycerol,” *Sci. Data*, vol. 10, no. 1, p. 894, Dec. 2023, doi: 10.1038/s41597-023-02819-3.

[95] V. Gupta *et al.*, “Advanced Colloidal Sensors Enabled by an Out-of-Plane Lattice Resonance,” *Adv. Photonics Res.*, vol. 3, no. 11, p. 2200152, 2022, doi: 10.1002/adpr.202200152.

[96] M. Daimon and A. Masumura, “Measurement of the refractive index of distilled water from the near-infrared region to the ultraviolet region,” *Appl. Opt.*, vol. 46, no. 18, pp. 3811–3820, Jun. 2007, doi: 10.1364/AO.46.003811.

[97] M. Serra-Prat, I. Lorenzo, E. Palomera, S. Ramírez, and J. C. Yébenes, “Total Body Water and Intracellular Water Relationships with Muscle Strength, Frailty and Functional Performance in an Elderly Population. A Cross-Sectional Study,” *J. Nutr. Health Aging*, vol. 23, no. 1, pp. 96–101, Jan. 2019, doi: 10.1007/s12603-018-1129-y.

[98] A. M. Stroh *et al.*, “Human adipose and skeletal muscle tissue DNA, RNA, and protein content,” *J. Appl. Physiol.*, vol. 131, no. 4, pp. 1370–1379, Oct. 2021, doi: 10.1152/japplphysiol.00343.2021.

[99] M. R. Pinheiro, V. V. Tuchin, and L. M. Oliveira, “Analysis of the experimental absorption spectrum of the rabbit lung and identification of its components,” *J. Biophotonics*, vol. n/a, no. n/a, p. e202300494, 2024, doi: 10.1002/jbio.202300494.

[100] L. Oliveira, A. Lage, M. Pais Clemente, and V. Tuchin, “Optical characterization and composition of abdominal wall muscle from rat,” *Opt. Lasers Eng.*, vol. 47, no. 6, pp. 667–672, Jun. 2009, doi: 10.1016/j.optlaseng.2008.12.005.

[101] L. Oliveira, A. Lage, M. P. Clemente, and V. V. Tuchin, “A simple mixture to enhance muscle transmittance,” in *Saratov Fall Meeting 2007: Optical Technologies in Biophysics and Medicine IX*, SPIE, Jun. 2008, pp. 162–172. doi: 10.1117/12.803978.